Accepted Manuscript

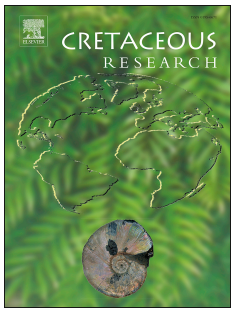

New insights into Cenomanian paleoceanography and climate evolution from the Tarfaya Basin, southern Morocco

Sebastian Beil, Wolfgang Kuhnt, Ann E. Holbourn, Mohamed Aquit, Sascha Flögel, El Hassane Chellai, Haddou Jabour

PII: S0195-6671(17)30217-3

DOI: 10.1016/j.cretres.2017.11.006

Reference: YCRES 3750

To appear in: *Cretaceous Research*

Received Date: 2 May 2017

Revised Date: 5 November 2017

Accepted Date: 7 November 2017

Please cite this article as: Beil, S., Kuhnt, W., Holbourn, A.E., Aquit, M., Flögel, S., Chellai, E.H., Jabour, H., New insights into Cenomanian paleoceanography and climate evolution from the Tarfaya Basin, southern Morocco, *Cretaceous Research* (2017), doi: 10.1016/j.cretres.2017.11.006.

New insights into Cenomanian paleoceanography and climate evolution from the Tarfaya Basin, southern Morocco

Sebastian Beil[1], Wolfgang Kuhnt[1], Ann E. Holbourn[1], Mohamed Aquit[1,2], Sascha Flögel[3], El Hassane Chellai[4] and Haddou Jabour[5]

[1]Institute of Geosciences, Christian-Albrechts-University, Ludewig-Meyn-Str.10-14, D-24118 Kiel, Germany

[2]OCP S.A., Direction de Recherche et Développement, Recherche Géologique, 46300 Youssoufia, Morocco

[3]GEOMAR Helmholtz-Zentrum für Ozeanforschung Kiel, Ozeanzirkulation und Klimadynamik, Paläo-Ozeanographie, Wischhofstr. 1-3, D-24148 Kiel, Germany

[4]Department of Geology, Faculty of Sciences Semlalia, Cadi Ayyad University, Marrakech, Morocco

[5]ONHYM, Office National des Hydrocarbures et des Mines, 5, Avenue Moulay Hassan, BP99 Rabat 10000, Morocco

Abstract

A 325 m long continuous succession of uppermost Albian to lower Turonian pelagic (outer shelf) deposits was recovered from a new drill site in the central part of the Tarfaya Basin (southern Morocco). Natural gamma ray wireline

logging, carbonate and organic carbon content, bulk carbonate and organic carbon stable isotopes and X-ray fluorescence (XRF)-scanner derived elemental distribution data in combination with planktonic foraminiferal biostratigraphy indicate complete recovery of the Cenomanian Stage. This exceptional sediment archive allows to identify orbitally driven cyclic sedimentation patterns and to evaluate the pacing of climatic events and regional environmental change across the Albian-Cenomanian boundary (ACB), the mid-Cenomanian Event (MCE) and Oceanic Anoxic Event 2 (OAE2) in the latest Cenomanian. The deposition of organic-rich sediments in the Tarfaya Basin, likely driven by upwelling of nutrient-rich water masses, started during the latest Albian and intensified in two major steps following the MCE and the onset of OAE2. The duration and structure of the MCE and OAE2 carbon isotope excursions exhibit striking similarities, suggesting common driving mechanisms and climate-carbon cycle feedbacks. Both events were also associated with eustatic sea level falls, expressed as prominent sequence boundaries in the Tarfaya Basin. Based on the 405 kyr signal imprinted on the Natural Gamma Ray (NGR) and XRF-scanner derived Log(Zr/Rb) records, we estimate the duration of the Cenomanian Stage to be 4.8 ±0.2 Myr.

Keywords: Oceanic Anoxic Event 2 (OAE2), mid-Cenomanian Event (MCE), Cenomanian, Cyclostratigraphy, Oxygen Minimum Zone (OMZ)

1. Introduction

Orbital control on greenhouse climate and sea level changes was previously associated with the 405 kyr eccentricity cycle and linked to well-documented fourth order sequences in marine sedimentary successions (e.g. Gale et al., 2008). An orbital control on these regularly paced cycles implies that they are not primarily caused by regional changes in subsidence or volcanic events, which occur episodically and are essentially non-cyclic in nature. A recent study suggested that Mesozoic greenhouse eustatic sequences and stable isotope records show a strong imprint of the ~2.4 Myr modulation of eccentricity cycle, implying that orbital forcing exerted a major control on sea level variations and on the carbon cycle in a greenhouse world (Boulila et al., 2011). These authors proposed that low insolation during minima in the ~2.4 Myr eccentricity modulation promoted Antarctic ice sheet expansion, which caused global sea level falls, expressed as sequence boundaries in the stratigraphic record. These climatic events were associated with perturbations of the global carbon cycle and gave rise to widespread deposition of organic-carbon rich sediments and carbon isotope excursions.

The late Albian to early Turonian interval provides an excellent case to test this hypothesis since it encompasses three major paleoceanographic events expressed as positive $\delta^{13}C$ excursions (the Albian-Cenomanian boundary excursion, the mid-Cenomanian Event and the latest Cenomanian OAE2). The $\delta^{13}C$ curve over these intervals is delineated by distinctive, globally correlated excursions in orbitally tunable sedimentary successions from several continents (Gale et al., 1999, 2002, 2008; Kuhnt et al., 2009). Most of the records are based on composites of correlated outcrop sections, which have high quality biostratigraphic control and allow detailed sedimentological observations.

However, continuously cored and logged drill cores that cover this time interval without major stratigraphic hiatuses in pelagic outer shelf environments are still extremely rare. Such continuous records are essential for detailed correlation of isotopic, oxygenation and sediment flux oscillations on a global scale and for resolution of late Albian to early Turonian climate, sea level and paleoceanographic evolution.

The chronostratigraphy of the Cenomanian Stage is still a matter of intense debate, despite a well established biostratigraphic framework based on planktonic foraminifers, calcareous nannoplankton and cosmopolitan ammonite taxa, in addition to carbon isotope stratigraphy and cyclostratigraphy. Gale (2007), Gale et al. (1999, 2002, 2008) and Kuhnt et al. (2009) used planktonic foraminifers, ammonites and carbon isotope stratigraphy to correlate Cenomanian eustatic sequences from southeast India, southern England, the US Western Interior and Morocco. Assuming that these sea level oscillations are driven by the long eccentricity (405 kyr) cycle in the Milankovitch frequency band, these authors came to the conclusion that the Cenomanian Stage encompasses 11 ±1 eccentricity cycles, corresponding to a duration of the Cenomanian Stage of 4.4 ±0.4 Myr. This estimate is in agreement with a study including sequence stratigraphy, cosmopolitan dinoflagellate biostratigraphy and ammonite biostratigraphy that correlates the base of the Cenomanian with the Clay Spur Bentonite Bed radiometrically dated at 97.88 ±0.69 Ma in the Western Interior, resulting in an age of 97.13 Ma for the base of the Cenomanian and a duration of just over 4 Myr for the Cenomanian Stage (Scott et al., 2009; Scott, 2014). However, this is in sharp contrast to the widely used Geological Timescale 2012 (Gradstein and Ogg, 2012), which approximates the duration of

the Cenomanian Stage to 6.6 ±0.6 Myr, based on Ar/Ar dates of bentonites in the Western Interior and Japan.

A key to integrate Cenomanian biostratigraphic events, cyclostratigraphy and carbon isotope stratigraphy lies in resolving the chronostratigraphic position of the globally recognized mid-Cenomanian carbon isotope excursion in relation to the well-established chronology across the Cenomanian-Turonian boundary and, thus, determine the duration of the late Cenomanian. Based on the dating of Obradovitch (1993), Gale et al. (2008) assigned a radiometric age of 95.78 ±0.61 Ma to a bentonite bed within the Thatcher Limestone Member, associated with the first $\delta^{13}C$ peak of the mid-Cenomanian carbon isotope excursion, which places the mid-Cenomanian event 2 Myr before or, in agreement with the cyclostratigraphy of Gale (2007), five long eccentricity cycles below the Cenomanian-Turonian boundary. However, high precision U-Pb zircon ID-TIMS dating of a late-middle Cenomanian bentonite in the Western Canada Foreland Basin, which correlates with the "X" bentonite of the US Western Interior (dated by Obradovitch with 94.93 ±0.53 Ma), yielded an age of 95.87 ±0.10 Ma (Barker et al., 2011). This dating suggests that the sanidine Ar/Ar ages of Obradovitch (1993) are considerably too young and that the time interval between the Cenomanian-Turonian boundary and the first peak of the mid-Cenomanian $\delta^{13}C$ excursion corresponds to ~2.8 Myr or seven long eccentricity cycles.

In this study, we analyze a 350 m continuously cored research well, which was drilled in December 2009 close to the depocenter of the Tarfaya-Laayoune Atlantic Margin Basin (southern Morocco), referred to in this work as the Tarfaya Basin. During the Albian to early Campanian, the Tarfaya Basin was located at

126 the southeastern margin of the Central North Atlantic, forming an unrestricted
127 embayment (e.g. Ranke et al., 1982; Patriat and Labails, 2006) within the
128 Western Tethys that recorded not only regional variability but also global
129 environmental changes in the marine realm.

130 Continuous subsidence resulted in the deposition of more than 700 m of
131 Upper Cretaceous sedimentary rocks. The 325 m long Cretaceous interval
132 recovered in Core SN°4 spans the lower Turonian to uppermost Albian
133 (Vraconian). Earlier research (Kuhnt et al., 1990; Kolonic et al., 2005) and new
134 model simulations (Fig. 1) indicate that the upper water column at this location
135 was highly depleted in oxygen and was located within one of the global hotspots
136 of organic matter burial during the late Cenomanian and early Turonian. This
137 continuous record provides a unique opportunity to reconstruct the variability of
138 a hemipelagic outer shelf sedimentary environment in high to intermediate
139 temporal resolution (typically 1 cm spacing or ~200 year temporal resolution for
140 the XRF-scanner records, and 40 cm spacing or ~5-8 kyr for discrete analysis of
141 stable isotopes) and to gain new insights into Cenomanian and early Turonian
142 climate evolution. This sediment archive can also be correlated with regional
143 records from more proximal settings (Kuhnt et al., 2009), thus providing better
144 constraints on the Cenomanian sea level history of the Tarfaya Basin in
145 comparison to the global eustatic curve.
146
147

2. Material and Methods

2.1 Core Tarfaya SN°4

Core Tarfaya SN°4 (N 27° 59' 46.4'', W 12° 32' 40.6'') was drilled with the assistance of ONHYM (National Office of Hydrocarbons and Mines of Morocco) in December 2009, ~40 km east of the town of Tarfaya, close to the road to Tan Tan. Core SN°4 is located between previously drilled wells S13 and S57/S75 (Fig. 2). The most complete exploration well S13, drilled in the 1970s by ONAREP close to the town of Tarfaya, did not recover the base of the Cenomanian and wireline logging was restricted to the Turonian and uppermost Cenomanian. Oil shale exploration wells (e.g. S57 and S75) drilled subsequently by Shell (Leine, 1986) focused on organic rich black shales and were terminated at the onset of OAE2.

A Salzgitter WD3500 hydraulic drilling system with metal core barrels (section length 3.05 m) and seawater as drilling liquid was used to recover Core SN°4. Each section was divided in segments of ~80 cm length, which were sealed in plastic sleeves. The diameter of the cores was 88 mm for the upper 120 m and 68 mm for the lower part down to the bottom at 350.2 m. Individual segments were cut with a Kaufmann-Titan diamond rock saw into working and archive halves. A few segments, which were too fragile to be sawed, appear as gaps in the linescan and XRF-scanner records. A new depth scale was created to compensate for discrepancies between cumulative section lengths measured during drilling (referred to as driller's depth) and cumulative segment lengths measured during XRF-scanning (Supplementary Material Table S1). For plotting analytical results and time series analysis the new depth scale was used.

2.2 Wire-line logging, Natural Gamma Ray

Wireline logging was carried out by Geoatlas Laayoune between 23 and 28 December 2009 immediately after the drilling operations were completed. The following suite of logging tools was used: (1) Natural Gamma Ray (NGR), values are given in counts per second (cps) as API (American Petroleum Institute) radioactivity units with a vertical resolution of 10 cm, (2) Caliper Log, (3) Downhole P- and S-wave velocity logging, (4) Normal Resistivity 16”N, 64”N, (5) Electric Log in mono-electrode and lateral configuration (RES), (6) Conductivity and resistivity of fluids, (7) Temperatures (absolute and differential), (8) Electromind Optical Televiewer Probe (OPTV). The walls of the hole were not covered with a metal casing and logging depth is recorded relative to the surface with a precision of ±0.1 m. However, the OPTV logging was carried out immediately after drilling and the strong turbidity and dispersed sediment in the drilling fluid did not allow to obtain high quality images.

2.3 Time series analyses

Harmonic analysis was performed using the astrochron-package (Meyers et al., 2012) for R (R Core Team, 2017). For Evolutive Harmonic Analysis (EHA), the *eha*-function of the astrochron-package (Meyers et al., 2012) with a window of 25 m and a step-size of 0.1 m for NGR and 0.01 m for the linearly interpolated and detrended Log(Zr/Rb) dataset was used in the frequency range between 0 and 1 cycles/m. Spectral analysis was performed with the *mtmML96*-function (Patterson et al., 2014) of astrochron, an implementation of the robust red noise MTM analysis of Mann and Lees (1996).

2.4 Biostratigraphy

Samples for biostratigraphy (10-120 g) were taken every ~5-10 m, dried, crushed and then treated for 3 to 5 days with the alcoholic solution of anionic tensides REWOQUAT W 3690 PG by REWO-Chemie (Steinau, Germany). Soaked samples were, then, washed with a 63 µm sieve, dried and sieved into the size fractions 63-150, 150-250, 250-630 and >630 µm. The size fraction 250-630 µm was used for the identification of planktonic foraminifers and foraminiferal biozones were defined following the zonation of Robaszynski and Caron (1995) with modifications across the Albian/Cenomanian boundary based on a detailed re-investigation of the Global Boundary Stratotype Section and Point (GSSP) for the base of the Cenomanian Stage at Mont Risou, France (Petrizzo et al., 2015). These recent investigations of the boundary stratotype now allow to discriminate a brief interval between the last occurrence of the late Albian *Planomalina buxtorfi* and the first occurrence of the early Cenomanian marker *Thalmanninella globotruncanoides* (which we lumped with *Thalmanninella brotzeni*), which is characterized by the occurrence of *Thalmanninella gandolfii* (Petrizzo et al., 2015). The sampling grid was subsequently refined to constrain the zonal boundaries.

2.5 Carbonate content, total organic carbon and nitrogen

Between 8 and 10 mg of pulverized and homogenized sample material (sampling grid is identical with $\delta^{13}C_{org}$ measurements) was sealed twice in tin capsules for Total Carbon (TC) and Nitrogen (N) measurements. The same amount was twice weighed into silver capsules and decarbonized with 0.25N hydrochloric acid (HCL) before sealing for Total Organic Carbon (TOC)

223 measurements. Both sets of samples were measured with a Carlo Erba
224 Proteinanalyzer NA1500 at Geomar Helmhotz Centre for Ocean Research (Kiel).
225 For calibration and monitoring of longterm stability, different weights of
226 Acetanilid (10.36% N, 71.09% C) and a certified soil standard BSTD1 (0.216% N,
227 3.5% C) were weighed and measured. Total Inorganic Carbon (TIC) were
228 calculated as TIC=(TC-TOC)*8.3333. A total of 352 discrete samples were
229 measured along the core for TOC, N and carbonate content. As carbonate data
230 show a good correlation (R^2 = 0.69) with XRF-scanner derived Log(Terr10/Ca)
231 values, Log(Terr10/Ca) was used to continuously track changes of carbonate
232 content in high resolution along the core.
233
234 ***2.6 Stable isotopes ($\delta^{18}O$, $\delta^{13}C_{carbonate}$, $\delta^{13}C_{org}$)***
235 Stable isotope measurements of bulk carbonate were conducted on
236 samples of 1 cm thickness with a spacing of 40 cm between 23 and 193 m and of
237 120 cm between 193 and 251 m. The interval spanning the onset of OAE2 (98–
238 115 m) was additionally analyzed with a spacing of 2 cm by Kuhnt et al. (2017).
239 Before grinding with an agate mortar, sample surfaces were carefully cleaned to
240 avoid contamination by drilling mud. Measurements were performed at the
241 Leibniz Laboratory for Radiometric Dating and Stable Isotope Research
242 (Christian-Albrechts-University, Kiel) on the Finnigan MAT 251 and 253 with
243 Carbo-Kiel-autosampler for automated individual acid treatment of carbonate
244 samples. Longterm accuracy is ±0.05‰ for $\delta^{13}C_{carbonate}$ and ±0.08‰ for $\delta^{18}O$. For
245 the calibration of results, two standards of the National Institute Bureau of
246 Standards and Technology (Gaithersburg, Maryland, US) NBS 20 and NBS 19 and

247 an internal standard were used. Results are reported as $\delta^{18}O$ and $\delta^{13}C_{carbonate}$ on
248 the PeeDee belemnite (PDB) scale.

249 Sample intervals for organic carbon $\delta^{13}C_{org}$ analyses vary between ~1.6 m
250 over the interval 23 to 65 m, ~40 cm over the interval 65 to 115.2 m, ~100 cm
251 over the interval 115.2 to 250 m and ~120 cm over the interval 250 to 350 m.
252 Approximately 1 to 3 mg of sample material was surface cleaned and ground.
253 Samples were decarbonatized with 10% HCL and agitated until visible reaction
254 stopped. Subsequently, 25% HCL was added for the dissolution of dolomitic
255 material and samples were agitated overnight. After at least 12 hours of
256 exposure, samples were five times neutralized with deionized water followed by
257 decanting. Finally, samples were dried at 40°C, ground and measured with a
258 Flash EA 2000 elemental analyser coupled online to a ThermoFinnigan Delta V
259 Plus mass spectrometer at the GeoZentrum Nordbayern (Erlangen). Results are
260 reported as $\delta^{13}C_{org}$ on the V-PDB (Vienna PDB) scale. For control of accuracy, an
261 internal standard calibrated to the international standards USGS 40 and USGS 41
262 was measured. Measurement accuracy is ±0.06‰ (1σ).
263

264 ***2.7 XRF-scanner derived elemental ratios, Linescan imaging and RGB records***

265 A second generation Avaatech X-ray fluorescence (XRF) scanner at the
266 Christian-Albrechts-University, Kiel was used to scan segments after polishing
267 with fine-grained sand paper and covering with 4 µm thick Ultralene foil.
268 Scanning was performed in 1 cm intervals with a vertical slit of 1 cm and a
269 horizontal slit of 1.2 cm. Three different tube voltage settings for 10, 30 and 50
270 kV were used (scanning parameter and scanned elements in Supplementary
271 Material Table S2). Some segments were too fragile to be scanned and appear as

gaps in the XRF record. Raw spectra were converted into element counts with the iterative least-square package "WIN AXIL batch" from Canberra Eurisys and the voltage-specific Kiel models. For the analysis logarithmic ratios of elemental counts were used to eliminate method-specific effects such as matrix effect or variation in rock density (Weltje and Tjallingii, 2008).

Linescan data were acquired from the polished surface of working halves with the Jai CV-L107 3 CCD color linescan camera installed in the Avaatech XRF-scanner at the Christian-Albrechts-University, Kiel. The camera is equipped with a Dichroic RGB beam-splitter prism (RGB-channels at 630, 535 and 340 nm) followed by 3 sensors with 2048 pixel. The downcore resolution is 143 ppcm. L*, a* and b* were calculated from the digital RGB-images.

2.8 Numerical modeling

Modeling was performed with the UVic Earth System Climate Model (UVicESCM), which consists of an ocean general circulation model (Modular Ocean Model, Version 2) coupled to a vertically integrated two dimensional energy-moisture balance model of the atmosphere, a dynamic-thermodynamic sea-ice model, a land surface scheme, a dynamic global vegetation model and a sediment model. The model is driven by seasonal variations in solar insolation at the top of the atmosphere and seasonally varying wind stress and wind fields (after Flögel et al., 2005). The coupled model has a resolution of 2° in longitude and 2° in latitude and conserves energy, water and carbon to machine precision without the use of flux adjustment (Meissner et al., 2012 and references therein). The physical components of the model are described in Weaver et al. (2001).

3. Results

3.1 Wireline logging (Natural Gamma Ray)

The NGR dataset (Fig. 3) is characterized by a longterm decrease from an average of 99.3 cps (lowermost 30 m) to 53.7 cps (uppermost 30 m). Pronounced short-term cyclicity with high amplitude fluctuations is evident in the NGR logging record between 25 m (top of Cretaceous sedimentation overlain by ~25 m Moghrabien) and 120 m below surface (Fig. 3). This upper part of the record can be easily correlated to published density and NGR records of previously drilled Tarfaya wells, in particular Cores S13, S57, and S75 for which biostratigraphic and cyclostratigraphic frameworks are available (Kuhnt et al., 1997, 2005; Tsikos et al 2004; Meyers et al., 2012). A wavelet power spectrum over the interval 25 to 125 m indicates an increase in sedimentation rate at ~84 m within the upper part of cycle 3 (following the cycle scheme of Kuhnt et al., 1997) (Fig. 3), which is close to the biostratigraphically defined Cenomanian-Turonian boundary (Tsikos et al., 2004; Kuhnt et al., 2005, 2017). The increase in sedimentation rates from ~6-7 to ~8-9 cm/kyr is reflected by an increase in the wavelength of the most robust cycle (corresponding to 405 kyr long eccentricity) from ~28 to ~32 m and an increase in the wavelength of the shortest prominent cycle (corresponding to 38 kyr obliquity) from ~2-3 to ~3-4 m (Fig. 3).

3.2 Core description, carbonate content, TOC and XRF-scanner based estimates of terrigenous components

320 The core was subdivided into 3 main lithological units and 9 subunits
321 based on visual description (Fig. 4A and 4B), carbonate and organic carbon
322 measurements and XRF-scanner derived Log(Terr10/Ca)-data (Fig. 5A).
323
324 ***3.2.1 Unit 1 (23.6 to 126.8 m)***
325 Unit 1 is characterized by low terrigenous content and cyclic fluctuations
326 in organic carbon vs. carbonate-rich intervals, forming couplets of 3 m ±0.3 m
327 thickness. Unit 1 is subdivided into 3 subunits, based on carbonate content,
328 organic carbon and bedding rhythm:
329 Subunit 1a extends from Section 12, Segment 1, 0 cm (23.6 m) to Section
330 32, Segment 2, 42 cm (77.53 m). It consists of brown to dark brown marlstones
331 alternating with lighter brownish limestones. Subunit 1a exhibits prominent
332 variations in XRF-derived Log(Terr10/Ca), considered a proxy for terrigenous
333 input which is negatively correlated to $CaCO_3$-content, with generally higher
334 mean (-1.2916, StDev = 0.2426) than the underlying subunit. Discrete
335 measurements (n=59) give a mean carbonate content of 61% and an average
336 TOC-content of 7.4%. The lower boundary of Subunit 1a at 77.53 m was defined
337 at the base of a light brownish limestone bed with a sharp contact to the
338 underlying dark brown marlstone, correlative to the center of cycle 5 in the
339 scheme of Kuhnt et al. (1997) (Fig. 4B).
340 Subunit 1b reaches from Section 32, Segment 2, 42 cm (77.53 m) to
341 Section 42, Segment 3, 34 cm (108.79 m). It consists of brownish to light
342 brownish marly limestones and marlstones with intercalated black shales and is
343 characterized by marked lithologic changes between dark and light layers. It also
344 exhibits a large small-scale variability (StDev = 0.2404) in Log(Terr10/Ca), but

with lower average values (mean = -1.4693) than the underlying and overlying subunits. Average carbonate content is 71% and mean TOC content is 9.3% (n=72). This subunit corresponds to the interval of main organic carbon accumulation in the Tarfaya Basin (termed "zone riche" in the 1970s by oil shale exploration geologists from Shell and ONAREP). Subunit 1b includes the globally recognized OAE2, which is characterized by a prominent positive carbon isotope excursion. The base of Subunit 1b is defined by a distinct lithologic change from light brownish marly limestone to dark laminated shales correlative to the base of cycle 1 in the scheme of Kuhnt et al. (1997) (Fig. 4B).

Subunit 1c ranges from Section 42, Segment 3, 34 cm (108.79 m) to Section 49, Segment 1, 45 cm (126.80 m). It consists of brownish marly limestones and marlstones that are partly (intervals of over 1 m thickness) laminated (mm-scale) and also show a large high frequency variability (StDev = 0.2510) of Log(Terr10/Ca) (mean = -1.2473). Average carbonate content (64%) and average TOC (6.3%) are lower than in Subunit 1b (n=28). A distinct trend towards lower terrigenous input and higher carbonate and organic carbon contents is evident within Subunit 1c and orbital-scale cyclicity is poorly developed. The boundary to the underlying Unit 2 is gradual, the two units mainly differ in the proportion of terrigenous input, which is substantially higher in Unit 2 (Fig. 4B).

3.2.2 Unit 2 (126.8 to 312.2m)

Unit 2 is mainly characterized by an elevated proportion of the terrigenous component and lower carbonate and organic carbon percentages. Carbonate contents increase stepwise from the bottom to the top of the unit. We

subdivided Unit 2 in 4 subunits, mainly based on the relative importance of the terrigenous and biogenic (carbonate and organic carbon) components. The globally recognized carbon isotope event MCE is situated close to the lithological boundary between Subunits 2b and c.

Subunit 2a extends between Section 49, Segment 1, 45 cm (126.795 m) and Section 63, Segment 1, 0 cm (166.41 m). It consists of brownish marly limestones to marlstones with intercalations of lighter limestones, laminated intervals and black shales with a maximum thickness of 40 cm. Medium scale variability is increased (StDev = 0.2836) around an elevated mean in Log(Terr10/Ca) of -1.0365. Average TOC concentrations decrease to 4.8% with mean carbonate content of 64% (n=34). The base of Subunit 2a is placed at the transition between brighter marly limestones above to darker, more clay-rich marlstones below (Fig. 4B).

Subunit 2b extends from Section 63, Segment 1, 0 cm (166.41 m) to Section 76, Segment 4, 16 cm (207.99 m). It is composed of brownish marlstones that become enriched in clays and show increasing Log(Terr10/Ca) towards the base and overall increasing carbonate content from ~30 to ~70% towards the top. The middle part between 176 m and 183 m includes lighter intervals with higher carbonate content. Intercalated are intervals of marly limestones, up to 70 cm thick, and laminated intervals with a maximum thickness of 40 cm. Average TOC-concentrations are in the range of 4.2% (n=35). The base of Subunit 2b correlates with an abrupt change from brighter marlstones above to darker blackshales below.

Subunit 2c ranges from Section 76, Segment 4, (207.99 m) to Section 98, Segment 3, 35 cm (271.31 m). It consists of lighter brownish to greyish

calcareous marlstones and marly limestones, up to 30 cm thick, with lighter limestones. The top of Subunit 2c is generally darker and the variability in Log(Terr10/Ca) is lower (StDev = 0.2692, mean = -0.5217) than in the lower part. The boundary to Subunit 2d is characterized by an abrupt decrease in clay content evident by the transition from greenish marlstones above to brownish marlstones below (Fig. 4B). Mean carbonate content is 45% and mean TOC is 2.2% (n=56).

Subunit 2d ranges from Section 98, Segment 3, 35 cm (271.31 m) to Section 113, Segment 2, 28 cm (312.2 m). It consists of greyish to greenish-brownish clay-rich marlstones and is generally darker than underlying Subunit 3a. Intervals of up to 2 m are characterized by higher Log(Terr10/Ca) due to enrichment of clays. The upper boundary of this subunit corresponds to an abrupt decrease in clay content, whereas the lower boundary is marked by an abrupt increase in clay content. Subunit 2d is characterized by small-scale variability (StDev = 0.1861, mean = -0.1373) of Log(Terr10/Ca), low average carbonate content of 27% and low mean TOC of 1.9%. The contact to the underlying Unit 3 is characterized by the abrupt end of intense visible bioturbation at the top of Unit 3 (Fig. 4B).

3.2.3 Unit 3 (312.2 to 350.2 m)

Unit 3 is characterized by large changes in terrigenous sediment supply expressed in high variability of carbonate contents between <20 and >70%. The unit consists mainly of brownish to greenish-brownish marlstones with intercalations of clay-rich marlstones and claystones. Intensely bioturbated or

laminated intervals are rare. Unit 3 is subdivided into 2 subunits, mainly based on changes in terrigenous content.

Subunit 3a ranges from Section 113, Segment 2, 28 cm (312.2 m) to Section 120, Segment 4, 54 cm (335.265 m). It is characterized by an abrupt increase in terrigenous material and consists of brownish, calcareous marlstones that are generally lighter with a higher carbonate content of 46% (n=19) and decreased Log(Terr10/Ca) (mean = -0.6270) compared to the underlying Subunit 3b. A darkening upward trend in color is observed. TOC is slightly higher than in the underlying and overlying units with an average of 3.7%. The lower boundary to Subunit 3b is positioned at the transition between intensively bioturbated light grey marlstones below and dark grey to black, partly laminated marlstones above (Fig. 4B).

Subunit 3b extends from Section 120, Segment 4, 54 cm (335.265 m) to the bottom in Section 126, Segment 5, 7 cm (350.34 m). It consists of dark brown to greenish-brown marlstones with intercalations of marly limestones to limestones and finely laminated intervals with a thickness of up to 20 cm in the lower part. The increase in Log(Terr10/Ca) reflects increasing clay content from the bottom to the top of the subunit. Average carbonate content (36%) and TOC (2.2%, n=13) is lower than in Subunit 3a.

3.3 Planktonic foraminiferal biostratigraphy

The top of the Cretaceous interval at 23.6 m in Core SN°4 falls within the *Whiteinella archaeocretacea* zone of Robaszynski and Caron (1995) and is, therefore, of latest Cenomanian to earliest Turonian age (Fig. 4A). The FO of the lower Turonian marker *Helvetoglobotruncana helvetica* appears to be globally

444 diachronous (Gale et al., 1993) and its appearance is delayed in the Tarfaya Basin
445 (Kuhnt et al., 2005). Thus, we assume that the upper part of the *Whiteinella*
446 *archaeocretacea* zone recorded in SN°4 is already well within the lower Turonian.
447 We place the transition between the *Whiteinella archaeocretacea* and *Rotalipora*
448 *cushmani* zones at 101.8 m (between 101.70 and 101.89 m) in Core SN°4 based
449 on the last occurrence of *Rotalipora cushmani* at 101.89 m. The boundary
450 between the *Rotalipora cushmani* and *Thalmanninella reicheli* zone is located at
451 ~195 m (between 191.08 and 199.43 m). The lower limit of the *Thalmanninella*
452 *reicheli* and upper boundary of the *Thalmanninella brotzeni* zone is at ~213.6 m
453 (between 213.49 and 213.69 m). The first occurrence of *Thalmanninella*
454 *globotruncanoides,* which we lumped with *Thalmanninella brotzeni,* is in Section
455 113, Segment 1, 0-4 cm at 311.13 m. This datum defines the base of the
456 Cenomanian in the GSSP at Mount Risou (Petrizzo et al., 2015). The
457 *Thalmanninella gandolfii* zone (partial range zone between the first occurrence
458 of *Thalmanninella gandolfii* and *Thalmanninella globotruncanoides*) is included in
459 the latest Albian. The boundary between the *Thalmanninella gandolfii* and
460 *Thalmanninella appenninica* zone, which is also characterized by the last
461 occurrence of *Planomalina buxtorfi* is placed at ~319 m (between 314.23 and
462 323.5 m) (Fig. 4B).
463
464 ***3.4 Organic carbon (C_{org}) content and C/N ratio***
465 TOC varies between 0.2 and 20.5% (Fig. 5B). The lowermost part of the
466 core (350.34–235 m) is characterized by low TOC and low variability (average
467 1.9%, StDev 0.98%), except for a substantial increase in TOC (average 4.3%)
468 between 334.5 and 319.7 m. In the overlying interval (235–115 m), TOC

469 increases to an average of 4.3%, followed by a further increase (average 6.9%)
470 until 105 m. Highest TOC of 20.5% is measured in the interval from 105 to 83.5
471 m, where variability is highest (average 10.3%, StDev 4.9%). TOC exhibits a
472 decreasing trend in the remaining part of the core (Fig. 5B).

473 The atomic ratio (C/N ratio, Fig. 5B) of organically bound carbon (C_{org})
474 against total nitrogen content measured on bulk material fluctuates around 15
475 below 236 m, except for two intervals with increased ratios between 259 and
476 271 m (average of 21) and between 319 and 335 m (average of 20.5). Above 236
477 m, the C/N ratio shows a gradual increase, reaching an average of 36 in the
478 uppermost 10 m. This longterm trend is interrupted by an interval with larger
479 fluctuations reaching values of ~43.5 between 115 and 85 m, which corresponds
480 to OAE2.

481

482 ***3.5 Isotope stratigraphy ($\delta^{13}C_{org}$ excursions)***

483 Carbon isotope values (Fig. 5B) of organic matter vary between -29.24
484 and -24.24‰. A background level of ~28.5‰ or lower is determined above 250
485 m. This background level is punctuated by two prominent isotope excursions at
486 224–196 m (MCE) and at 107–65 m (OAE2). Both events are characterized by a
487 short negative excursion and a steep increase culminating in two peaks divided
488 by a transient decrease to lower values. The OAE2 $\delta^{13}C_{org}$ maxima are centered at
489 103.22 m (-24.20‰) and at 99.80 m (-24.31‰). The MCE exhibits $\delta^{13}C_{org}$
490 maxima at 211.99 m (-27.28‰) and 206.07 m (-26.80‰). Apart from their
491 different amplitude (1.7‰ for the MCE and 4.3‰ for OAE2), both isotope events
492 differ in the relative length of their plateau phase. OAE2 exhibits a longer lasting
493 plateau after the second $\delta^{13}C_{org}$ peak before values gradually return to

494 background levels. OAE2 additionally shows a third peak at the end of the
495 plateau at 88.7 m with a maximum of -25.1‰. The relative extent of the recovery
496 phases is also different, with a much faster return to background levels after the
497 MCE.

498 A third lower amplitude excursion corresponding to the Albian-
499 Cenomanian boundary event (ACB) occurs in the lower part of the core starting
500 with a sharp increase at 339 m from a late Albian background mean of -28.2‰
501 to a maximum value of -27.1‰, followed by a stepwise decrease to -28.1‰ at
502 318.5 m. Although the amplitude of the carbon isotope excursion marking the
503 ACB is only in the range of ~1‰, it is associated with an interval of TOC
504 enrichment and Log(Mn/S) depletion indicating an anoxic phase.

505

506 ***3.6 Bulk carbonate $\delta^{18}O$***

507 Oxygen isotope values (Fig. 5B) vary between -5.5 and -2.28‰ with high
508 amplitude short-term variability. Higher values occur predominantly between
509 251 and 106 m with an average of -3.64 ‰ and variations between -4.94 and -
510 2.28‰. The upper part of the record between 106 and 23 m is characterized by
511 lower values with an average of -4.12‰ (-5.65 to -2.28‰), following a decrease
512 that coincides with the $\delta^{13}C_{org}$ increase marking the onset of OAE2. Positive
513 excursions are recorded during OAE2 (starting at 102.73 m) of ~1.37‰ and
514 during the MCE (starting at 209.83 m and culminating at 206.07 m) of ~0.7‰.
515 The cross plot of bulk carbonate $\delta^{18}O$ against $\delta^{13}C$ over the interval analyzed for
516 stable isotopes does not reveal any significant correlation (Supplementary
517 Material Figure S3), supporting the interpretation of longterm trends as primary
518 features (Nelson and Smith, 1996). A detailed discussion of high frequency

519 variability of bulk stable isotopes for the OAE2 interval is included in Kuhnt et al.
520 (2017).
521
522 ***3.7 XRF-scanning derived elemental ratios***
523 We used four records of elemental ratios to characterize variations in
524 terrigenous input, proximity to the sediment source, clay mineral composition
525 and weathering in the source area and redox conditions at the sediment surface.
526
527 *3.7.1 Log(Terr10/Ca)*
528 The elements Al, Fe, K, Si and Ti generally have a terrigenous origin,
529 especially in hemipelagic settings (Peterson et al., 2000; Calvert and Pedersen,
530 2007; Mulitza et al., 2008; Tisserand et al., 2009; Govin et al., 2012). Tests of
531 marine organism contribute most of the calcium in the form of calcium carbonate.
532 The logarithmic ratio of the sum of Al, Fe, K, Si and Ti normalized against Ca
533 (Log(Terr10/Ca)) is, thus, used as a proxy for terrestrial clastic material vs.
534 marine biogenic carbonate (Fig. 5A).
535 In Core SN°4, values vary between -2.14 and +1.68 (Fig. 5A). Below
536 196.62 m (Subunits 3b to 2b), Log(Terr10/Ca) is characterized by increased
537 variability and overall higher values (>0.75). This is followed by a two-step
538 decline with a largest decrease occurring up to 166.41 m (Subunit 2b) and a
539 smaller decrease up to 108.79 m (Subunits 2a and 1c). The interval above 108.79
540 m shows large variability around a near constant average (<-1).
541
542 *3.7.2 Log(Zr/Rb)*

543 The element Zr is almost exclusively found in the heavy mineral
544 zirconium within sediments. Alumosilicates and their weathering products
545 (clays) are the main source for Rb. According to Calvert and Pedersen (2007)
546 high Log(Zr/Rb) ratios (sediments relative enriched in Zr) coincide with large
547 grain sizes due to the high density of zircons, which can only be transported in
548 conjunction with comparatively large grains of less dense minerals
549 (alumosilicates and quartz grains). In this study, Log(Zr/Rb) is interpreted as an
550 indicator of grain size changes in the terrigenous component due to changes in
551 the proximity of the sediment source, likely associated with sea level changes.
552 In Core SN°4, Log(Zr/Rb) varies between -0.82 and 1.41 (Fig. 5A). Despite
553 the large variability, Log(Zr/Rb) shows a clear cyclicity of ~4 m especially in the
554 lower part of the core below 196 m (Fig. 5A). Log (Zr/Rb) varies in antiphase
555 with Log(Terr10/Ca) between 348 and 337 m and between 312 and 275 m,
556 indicating extended periods of predominantly fine grained terrigenous discharge.
557 Above 196.62 m, short-term fluctuations in Log (Zr/Rb) decrease in amplitude
558 with longterm averages of ~0.6 between 196.62 and 86 m and of ~0.55 above 86
559 m.
560
561 *3.7.3 Log(K/Al)*
562 Log(K/Al) (Fig. 5A) has been widely used as a proxy for the mineralogical
563 composition of clay assemblages (Weaver, 1967, 1989; Niebuhr, 2005). We
564 interpret Log(K/Al) as reflecting variations in the amount of potassium-rich illite
565 in the clay mineral assemblages, which is controlled by variations of the
566 weathering intensity in the source area (Calvert and Pedersen, 2007). Silicate
567 weathering under warm conditions with sufficient supply of water is

568 characterized by a continuous breakdown of the crystal structure of feldspars
569 and a depletion of potassium in comparison to aluminum. Potassium-enriched
570 clay minerals in the tropics, thus, indicate relatively dry conditions in the source
571 area.

572 In Core SN°4, the log-ratio of K/Al varies between 0.3 and 1.3 except for a
573 few brief intervals with extreme potassium enrichment or depletion (Fig. 5A). As
574 for Log(Zr/Rb), Log(K/Al) exhibits high amplitude variability with a wavelength
575 of >~4 m in the lower part of the core (>196.62 m). The lowermost interval (270-
576 350 m) also shows characteristic minima in Log(K/Al) around 275-312 m and
577 337-348 m. Between 202 and 270 m, Log(K/Al), unlike Log(Zr/Rb), shows a
578 pronounced longterm minimum (mean values ~0.6) that ends with a marked
579 increase at 202 m. Above 202 m, Log(K/Al) shows a stepwise increase in average
580 values from 0.85 between 202 and 87 m to 0.95 between 87 and 23 m. This
581 stepwise trend is paralleled by a decrease in amplitude recorded in decreasing
582 standard deviation from 0.132 (202–87 m) to 0.099 (above 87 m).

583

584 *3.7.4 Log(Mn/S)*

585 The main factor controlling Log(Mn/S) (Fig. 5A) is deep water
586 oxygenation and the redox state at the sediment-water-interface, as manganese
587 (Mn) is insoluble under oxic conditions, but soluble under reducing conditions
588 (Landing and Bruland, 1980; Bruland, 1983). As shown by Brumsack (2006), Mn
589 is generally depleted in modern and Cretaceous sediments underneath upwelling
590 zones. Sulfur content is mainly influenced by the degree of pyritization in normal
591 pelagic sediments, which is to a certain degree controlled by the TOC content and
592 reactivity of the organic matter (Rachold and Brumsack, 2001). Sediments

593 depleted in sulfur in combination with a low organic matter content are
594 indicative of well-oxygenated bottom water conditions (Rachold and Brumsack,
595 2001). Log(Mn/S) is, therefore, interpreted as an indicator for bottom water
596 oxygenation with an increased ratio indicative of better ventilated bottom water.
597 In Core SN°4, Log(Mn/S) generally varies between -2 and 0, except for a
598 few levels enriched with pyrite crystals (Fig. 5A). Between 350 and 320 m,
599 Log(Mn/S) fluctuates from -1.2 to -1.6 with an interval of sustained lower values
600 (~-1.5) between 333 and 326 m. The interval 320–273 m is characterized by
601 higher values (>-1) and lower amplitude variability. Between 273 and 185 m,
602 Log(Mn/S) exhibits a longterm decrease in values and amplitude. In the upper
603 part of the core (185–23 m), Log(Mn/S) displays relatively low amplitude
604 variability, oscillating around a mean of ~-1.6.
605
606 ***3.8 Cyclostratigraphy based on NGR logging and XRF-scanner elemental***
607 ***ratios***
608 Cycles with a wavelength of >100 m were removed from the NGR dataset
609 using the *astrochron*-function *noKernel* (Meyers et al., 2012). EHA of the filtered
610 NGR data reveals strong cyclicity with high amplitude variability in the upper
611 part of the core between 60 and 110 and lower amplitude variability over the
612 intervals 150 to 230 m and 280 to 337.5 m (Fig. 6, Supplementary Material
613 Figure S4). Within the high amplitude interval between 60 and 110 m, a highly
614 significant peak (confidence level (CL) > 95%) is determined by spectral analysis
615 (Table 1) with frequency of 0.2474 cycles/m (wavelength 4.04 m). Additional
616 significant peaks (CL > 90%) are at 0.03198 (31.33 m) and 0.47087 (2.12 m)

617 cycles/m. Power-maxima at 0.14765 (6.77 m), 0.33121 (3.02 m) and 0.70231
618 (1.42 m) cycles/m are not statistically significant.

619 The XRF-scanner derived Log(Zr/Rb) shows strong cyclicity below 200 m
620 (Fig. 7). The record above ~200 m exhibits considerably lower amplitude
621 variability. We restricted the spectral analysis of the Log(Zr/Rb) record to the
622 interval between 200 and 350 m, which exhibits the strongest signal. Low
623 frequency cycles with a wavelength of >100 m detected mainly in the lower part
624 of the core were removed using a Gaussian kernel in the astrochron-function
625 *noKernel* (Meyers et al., 2012). Spectral analysis of Log(Zr/Rb) indicates
626 statistically highly significant (>99, 95 and 90 % confidence level) spectral peak
627 at periodicities of 46.96, 21.47, 14.45 and 9.16 m, related to fluctuations in the
628 grain density and grain size of the terrigenous component (Fig. 7). Additional
629 peaks centered at 5.3 m (0.19032 cycles/m), 3.1 m (0.31809 cycles/m) and 1.6 m
630 (0.62686 cycles/m) (Table 2) are statistically less significant (CL<90%).
631
632
633 **4. Discussion**
634
635 ***4.1 Late Albian-early Turonian orbital variability***
636 Despite decades of research, a definitive orbital solution for the time
637 period older than 40 Ma still remains elusive. The solution of Laskar et al. (2004,
638 La04) includes the full orbital parameter set of precession, obliquity and
639 eccentricity, but is only valid for the last 40 Ma. Laskar et al. (2011a) published a
640 more extended solution with four different options, but it was limited to
641 eccentricity (Fig. 8). Furthermore, these authors stressed that due to the chaotic

642 behavior of the inner solar system and limitations in the knowledge of the tidal
643 dissipation effect, shorter orbital periodicities (precession and obliquity) could
644 not be extended beyond the scope of the La04 solution. Thus, further
645 refinements of orbital solutions need to be based on comparisons with
646 sedimentological records (Laskar et al., 2011b). Only periodicities caused by the
647 interactions of planets in the outer planetary system are stable enough to allow a
648 projection into the deeper past (Laskar et al., 2011a, 2011b). However, the long
649 modulation of eccentricity with a wavelength of 405 kyr was considered to be
650 stable and valid for paleoceanographic reconstructions (Laskar et al., 2004,
651 2011a, 2011b, Fig. 8), even for periods of 100 Ma and beyond. Although the
652 chaotic character governing the motion of celestial bodies of the inner solar
653 system and especially the motion of large asteroids may prevent the calculation
654 of a definitive orbital solution for periods beyond the Cenozoic (Laskar et al.,
655 2011b), the relative ratio of different frequencies are still suitable for deeper
656 time intervals (Berger et al., 1992). These ratios can be used for the analysis of
657 power spectra of sedimentary sequences (e.g., Meyers and Sageman, 2007).
658

659 ***4.2 Identification of orbital periodicities in NGR and Log(Zr/Rb) records***

660 Prominent cycles in NGR over the interval 60 to 110 m in Core SN°4,
661 which encompasses OAE2, allow analysis and correlation of power maxima with
662 distinct frequencies (Fig. 6 and Table 1), based on the ratio between the
663 respective orbital wavelengths extracted from the orbital solutions La2004,
664 2010a-d and 2011 (Laskar et al., 2004, 2011a and 2011b). Highly significant
665 peaks correlate to long eccentricity (E1) with wavelength of 31.33 m, to obliquity
666 (O1) with wavelength of 4.04 m and to precession (P1) with wavelength of 2.12

667 m. Additional peaks interpreted as short eccentricity (E3) with wavelength of
668 6.77 m, O2 with wavelength of 3.02 m and P2 with wavelength of 1.42 m support
669 this interpretation. The calculated sedimentation rate based on the long
670 eccentricity cycle (405 kyr) is 7.7 cm/kyr. This agrees well with the calculated
671 sedimentation rates of 8.47 and 6.07 cm/kyr for nearby Core S13 in the Tarfaya
672 Basin (Meyers et al., 2012).

673 Strong cyclicities in Log(Zr/Rb) below 200 m (Fig. 7) permitted further
674 analysis in the lower part of the core. The correlation with orbital frequencies
675 extracted from the La2004 (precession, obliquity and eccentricity) and
676 La2010/2011 solutions (eccentricity) reveals the most significant frequencies
677 between 14.45 m and 21.47 m wavelength, which corresponds to 321 and 477
678 kyr respectively and, thus, represents the long (405 kyr) eccentricity cycle. The
679 relatively broad double peak is most likely caused by changes in sedimentation
680 rate within the analyzed window of 200 to 350 m. Thus, the average 405 kyr
681 cycle has a wavelength of 18 m (frequency of 0.055 cycles/m) assuming an
682 average 4.5 cm/kyr sedimentation rate with sedimentation rates varying
683 between 3.6 and 5.3 cm/kyr. Obliquity cycles vary between 1.6 and 3.14 m,
684 depending on sedimentation rates and varying spectral power of the 38 and 48
685 kyr obliquity cycles (Table 1). The short eccentricity cycle has a relatively
686 consistent wavelength of ~5.25 m (corresponding to 117 kyr at average
687 sedimentation rate of 4.5 cm/kyr). Based on an average sedimentation rate of 4.5
688 cm/kyr for the interval between 200 and 350 m, the duration of the lower
689 Cenomanian (thickness of 120 ±10 m) is estimated to be 2.66 ±0.2 Myr.

690 The strongest and most significant frequency in the NGR data occurs
691 between 60 and 110 m (frequency of 0.24741 cycles/m, 4.04 m wavelength) and

692 corresponds to O1 (48.54 kyr) (Fig. 6), implying a strong obliquity forcing on
693 depositional processes, even at low latitudes during the late Cenomanian.
694 However, the mechanism translating obliquity forcing into a signal imprinted on
695 low latitude sediments remains enigmatic. Possible processes may include mean
696 annual insolation in the tropics, which decreases with higher obliquity, and
697 obliquity-driven changes in the insolation gradient between high and low
698 latitudes, which enhances seasonal atmospheric heat and moisture transfer
699 between high and low latitudes, especially in a supergreenhouse world. Recently,
700 Laurin et al. (2015) suggested an alternative mechanism, albeit effective only on
701 longer timescales. These authors used modeling in comparison with proxy data
702 to reproduce the 1.2 Myr obliquity modulation during the Late Cretaceous, based
703 on non-linear responses of high-latitude (e.g. peats, permafrost, methane
704 hydrates) and global (euxinic basins, soils) carbon reservoirs to insolation
705 forcing. These authors suggested that destabilization of these reservoirs in
706 combination with reconfiguration of the global circulation strongly influenced
707 the global marine carbon cycle.

708 A general characteristic of the EHA of NGR (Fig. 6) is the unusually strong
709 cyclicity signal during OAE2. In contrast, the upper part of the MCE interval (195-
710 210 m) is characterized by a muted orbital signal (Supplementary Material
711 Figure S4). The orbital signal between the ACB and the early phase of the MCE
712 including the first $\delta^{13}C_{org}$ maximum remains weak. Assuming that bottom water
713 dysoxia or anoxia facilitates the preservation of the original orbital signal in
714 sediments due to the lack of bioturbation, the low TOC-content measured for the
715 MCE suggests an attenuation of the signal by bioturbation and therefore at least
716 dysoxic conditions at the sea floor. An alternative explanation is that the sea level

717 fall connected to the sequence boundaries Ce2.1 and Ce3 (chapter 4.6) are
718 responsible for considerable short-term changes in sedimentation rates, which
719 would obliterate clear orbital patterns in the sedimentary record.
720 The general stronger response to orbital forcing during OAE2, as detected
721 with EHA, may be caused by enhanced preservation of the cyclic sedimentary
722 structure due to reduced bioturbation and predominance of laminated deposits.
723 Further possible influences on the response to orbital forcing include high
724 frequency fluctuations in sea level and pCO_2 or a generally higher response of the
725 Oxygen Minimum Zone (OMZ) to organic carbon flux at higher deep water
726 temperatures. Sea level would control transport distance of deposited sediments,
727 smooth short-term variability with increasing sea level and decreasing proximity
728 and, therefore, transfer power from short-term to longer term periodicities.
729 Global warming under increasing atmospheric pCO_2 may have, thus, intensified
730 the imprint of orbital variability by modifying intermediate water oxygenation
731 and sediment input.
732
733 ***4.3 Evolution of bottom water oxygenation, organic matter accumulation***
734 ***and paleoproductivity***
735 Changes in bottom water oxygenation and organic matter accumulation
736 are approximated from TOC, C/N and Log(Mn/S). Lower Cenomanian deposits
737 (between 273 and ~320m) in Core SN°4 are generally characterized by high
738 Log(Mn/S), and low TOC (<3 %), indicative of relatively well ventilated bottom
739 water conditions (Fig. 5). In the latest Albian (below ~320 m), higher TOC values
740 (3-8%) and lower Log(Mn/S) values (in the range of -1.2 to -1.6 with strong
741 fluctuations in the lower part) indicate more dysoxic/anoxic conditions in the

742 water column. In particular the interval 333–326 m, where Log(Mn/S) is
743 consistently lower (fluctuating around -1.5, comparable to values in the upper
744 Cenomanian/Turonian), corresponds to a transient period of anoxia and
745 elevated organic matter accumulation. A coeval increase in organic matter (TOC
746 fluctuating at ~5%) supports the interpretation of oxygen-depleted conditions
747 promoting improved preservation of organic matter during this interval.
748 Log(Mn/S) exhibits an extended transitional phase between ~185 m and
749 273 m with strongly fluctuating Log(Mn/S) and a consistent decrease in mean
750 values from ~-1.0 to ~-1.5. This transitional trend in Log(Mn/S) is paralleled by
751 TOC, which increases from a running mean of ~2 to ~5%. Above ~185 m,
752 Log(Mn/S) becomes more stable around a mean of -1.5 and high amplitude
753 fluctuations (>–1.3) become rare transient events. We interpret this evolution as
754 indicative of the establishment of an increasingly stable OMZ during a long
755 transitional phase between 185 and 273 m. This transition towards less
756 oxygenated conditions may have been facilitated by a regional sea level rise that
757 promoted impinging of the OMZ on the shelf. The interval <185 m is
758 characterized by prevailing anoxic bottom water conditions with only transient
759 oxygenation events. The establishment of a stable late Cretaceous OMZ in the
760 latest Cenomanian/early Turonian is a common feature along the West African
761 Margin (e.g., Holbourn et al., 1999). However, our data suggest that the transition
762 towards an upwelling-related oxygen depleted depositional environment started
763 earlier (in the middle part of the early Cenomanian at 273 m in Core SN°4) in the
764 Tarfaya Basin and resulted in consistent deposition of organic-rich sediments
765 since the end of the middle Cenomanian (~185 m). Although both the upper
766 Albian and OAE2 are characterized by elevated TOC in the Tarfaya Basin, the

MCE is not characterized by exceptional changes in oxygenation or TOC accumulation at a time when the "background" oxygen depletion and resulting organic matter preservation were already elevated in the Tarfaya Basin.

4.4 Mid-Cenomanian Event (MCE): A precursor to OAE2?

The MCE, originally defined in the chalk successions of northwestern Europe (Paul et al., 1994), was subsequently identified in different ocean basins and is now considered a global event (Mitchell et al., 1996; Mitchell and Carr, 1998; Jarvis et al., 2001, 2006; Coccioni and Galeotti, 2003; Voigt et al., 2004; Gale et al., 2008; Hardas et al., 2012; Giraud et al., 2013). In Core SN°4, the MCE is characterized by a positive carbon isotope excursion with an increase in $\delta^{13}C_{org}$ of ~1.7‰ and a characteristic double peak within the *T. reicheli* Zone. A $\delta^{13}C_{org}$ minimum immediately precedes the main positive shift (Fig. 5). These features show striking similarities to the shape of the $\delta^{13}C_{org}$ curve across OAE2, which was studied at higher resolution in SN°4 by Kuhnt et al. (2017). The SN°4 records also indicate that the duration of the early phase (negative excursion, main increase and double peak) of the MCE and OAE2 isotope events was comparable, taking into account differences in sedimentation rate (7-8 cm during OAE2 and ~4 cm during the MCE). In both cases, the duration of this early phase corresponds to one long (405 kyr) eccentricity cycle, suggesting that the onset and early development of the MCE and OAE2 were orbitally modulated.

The MCE and OAE2 both exhibit short-lived increases in $\delta^{18}O$ following the initial $\delta^{13}C_{org}$ increase. The $\delta^{18}O$ increase during OAE2 was attributed to a massive atmospheric CO_2 drawdown through organic matter burial (e.g. Jarvis et al., 2011), which resulted in global cooling, as indicated by different proxies in

792 various basins (e.g. Forster et al., 2007; Pearce et al., 2009; Barclay et al., 2010).
793 A sustained cooling phase that may have even resulted in ephemeral glaciations
794 in Antarctica, was also suggested for the MCE based on a bulk carbonate $\delta^{18}O$
795 increase in combination with sequence stratigraphic evidence for a high-
796 amplitude sea level fall (Stoll and Schrag, 2000; Miller et al., 2003, 2005). A
797 significant cooling during the MCE was determined from brachiopod shells from
798 the mid-latitudinal shelf of Europe by Voigt et al. (2004). These authors hesitated
799 to relate the cooling with ephemeral glaciations because the coolest
800 temperatures were determined within a bed identified as a transgressive surface,
801 preferring the alternative explanation of a major re-organization of shelf sea
802 circulation. A temperature minimum expressed as a $\delta^{18}O$ maximum, also occurs
803 above a transgressive surface in Core SN°4 (Fig. 9), although initial cooling
804 started significantly earlier following the first $\delta^{13}C_{org}$ peak within the MCE.
805 Maximum cooling coincided with the second $\delta^{13}C_{org}$ peak, as in the Contessa
806 record (Stoll and Schrag, 2000), but unlike the Salder record (Voigt and Hilbrecht,
807 1997). The widespread occurrence of these events thus suggests a supra-
808 regional or even global character rather than a regional re-organization of shelf
809 circulation.

810 The "mid-Cenomanian glaciation hypothesis" was subsequently
811 challenged by isotope records of glassy planktonic and benthic foraminifers that
812 did not indicate a measurable ice volume signal in $\delta^{18}O$ records across the MCE
813 (Moriya et al., 2007; Ando et al., 2009). However, the isotopic composition of
814 Antarctic ice in the Cretaceous greenhouse world must have been relatively close
815 to or even heavier than that of modern "warm" Greenland ice (in the order of -25
816 to -30‰ in contrast to today's Antarctic ice $\delta^{18}O$ of -55‰, Lhomme et al., 2005).

817 Thus, even the waxing and waning of sizable ice caps with a sea level effect in the
818 order of 20-30 m (half of the modern Antarctic ice shield) would probably not be
819 detectable in Cretaceous marine $\delta^{18}O$ records.

820 Apart from striking similarities, there are also differences between the
821 MCE and OAE2. In particular, the amplitude and shape of the $\delta^{13}C_{org}$ excursion as
822 well as the organic carbon burial rates differ markedly. In contrast to the
823 characteristic plateau and gradual $\delta^{13}C_{org}$ decrease in the later stage of OAE2, the
824 end of the MCE carbon isotope excursion is relatively abrupt and $\delta^{13}C_{org}$ returns
825 rapidly to background level. However, the similarities in the carbon isotope
826 record and associated sedimentation patterns during the onset of the MCE and
827 OAE2 suggest comparable triggering mechanisms and climate-carbon cycle
828 feedbacks during the two events, although the duration and amplitude of the
829 initial CO_2 release from volcanic exhalations and the amount of ^{12}C sequestered
830 through organic carbon burial probably were considerably lower during the MCE
831 than during OAE2.

832 In contrast to that of the MCE, the OAE2 $\delta^{18}O$ record additionally shows a
833 pronounced temperature increase towards a stable global Turonian temperature
834 optimum, which is approximately in phase with the $\delta^{13}C_{org}$ increase (Clarke and
835 Jenkyns, 1999; Wilson et al., 2002). Based on osmium isotope data, Turgeon and
836 Ceasar (2008) and Du Vivier et al. (2014) suggested that this global temperature
837 increase was related with volcanic exhalations of the Columbia-Caribbean Large
838 Igneous Province. Modeling studies (e.g. Flögel et al., 2011) further supported
839 the notion of volcanogenic CO_2-induced warming into the Cenomanian-Turonian
840 climate optimum.

841

4.5 Timing of $\delta^{13}C$ excursions and duration of the Cenomanian Stage

In Core SN°4, the initial $\delta^{13}C$ increases defining the onset of the three main anoxic events are located at 107 m (OAE2), 217 m (onset of the MCE) and 339 m (ACB), resulting in depth differences of 110 m between OAE2 and the MCE and of 122 m between the MCE and the ACB. Mean sedimentation rates for these intervals, estimated from the dominant orbital cycles (from 14.45 to 21.47 m for the 405 kyr long eccentricity cycle), are between 3.6 and 5.3 cm/kyr, with an overall average of 4.5 cm/kyr in the lower part of the core and typically 7.7 cm/kyr (31.33 m for a 405 kyr long eccentricity cycle) in the upper part of the core during OAE2. Changes in the frequency spectrum and signal amplitude in the EHA of NGR indicate a change in sedimentation rates at a depth of ~120 m (Fig. 6). Decreasing Log(Terr10/Ca) and increasing carbonate content also point to higher accumulation rates of carbonate (Fig. 5A). An increase in primary production and biogenic flux is also evident in the TOC record, which registers a marked increase above ~120 m. For an estimate of the time interval between the onset of the MCE and OAE2 we use the sedimentation rate of 7.7 cm/kyr, characteristic of enhanced carbonate/organic carbon accumulation, for the depth between 107 and 120 m, which results in a duration of ~0.17 Myr for this 13 m interval. The remaining 97 m (between 120 and 217 m) were deposited at an average sedimentation rate of 4.5 cm/kyr, in ~2.16 Myr adding up to a total duration of ~2.33 Myr for the interval between OAE2 and the MCE, which is close to the modulation of the long eccentricity cycle (~2.4 Myr).

The time difference between the MCE onset (217 m) and the ACB (339 m) calculated with sedimentation rates of ~4.5 cm/kyr corresponds to 2.71 Myr, which is again within the range of the 2.4 Myr modulation of the long eccentricity

867 cycle. Together these estimates suggest a duration of ~4.8 Myr for the
868 Cenomanian Stage, since the ACB with a duration of one 405 kyr eccentricity
869 cycle still falls into the latest Albian and the main part of OAE2 with
870 approximately the same duration occurs in the Cenomanian. A minimal tuning
871 approach using calculated sedimentation rates is presented in Supplementary
872 Material Figure S5. Filtering for 405-kyr-cyclicity resulted in 11 long eccentricity
873 cycles in agreement with Gale et al. (1999). These results support the estimated
874 duration of the Cenomanian Stage suggested by Gale et al. (1999) and are in
875 contrast to the significantly longer duration proposed by Gradstein et al. (2012).
876
877 ***4.6 Correlation of Cenomanian eustatic sea level records***
878 Previous studies of sedimentary successions in the Tarfaya Basin included
879 sequence stratigraphic interpretations of sedimentary features in outcrop
880 sections situated in the more proximal part of the basin (Kuhnt et al., 2009; Aquit
881 et al., 2013, 2015). These studies identified sequence boundaries and
882 transgressive surfaces as important sequence stratigraphic features for
883 interbasinal correlations of past sea level changes (Haq, 2014) and tentatively
884 correlated them to the Cenomanian eustatic sea level reconstruction of Gale et al.
885 (2002, 2008). Transgressive surfaces (TS) form the first significant flooding
886 surface at the onset of a transgressive sequence. The TS develops, when the
887 increase in accommodation space outpaces the rate of sediment supply, thus
888 forming the base of the transgressive systems tract (TST). A TS is often
889 characterized by well cemented carbonate surfaces or hard grounds, which are
890 commonly perforated by burrowing organisms.

In shallow shelf sedimentary systems or areas with low sediment supply, where falling sea level and/or lowstand facies is not usually preserved above the sequence boundary, the TS falls together with the sequence boundary (SB). Following this approach, Kuhnt et al. (2009) interpreted the characteristic nodular limestone beds in the more proximal section at Mohamed Plage as transgressive and merged the TS and SB at the base of these limestone beds. However, in the more distal Core SN°4, we consider that the relatively coarse grained carbonate beds or nodules in this deeper environments represent lowstand deposits between the SB and the TS. Sedimentary rocks across and immediately overlying the TS are commonly coarse-grained and winnowed by waves or tidal currents in deeper marine settings. These features are recognizable in our continuous XRF-scanner records by peaks in the Log(Zr/Rb) that are accompanied by low Log(Terr10/Ca), whereas high Log(Terr10/Ca) are more typical for fine-grained clay mineral deposition. On the NGR curve, a TS typically consists of a relatively abrupt increase in NGR associated with deposition of organic rich shales during the transgressive system tract above the TS.

Following these criteria, we identified five major TS within the sedimentary succession of Core SN°4 (Fig. 9 and Supplementary Material Figure S6):

(1) A major TS is recognized at 105 m within the onset of OAE2, which is correlative to sequence boundary Ce5 in the nomenclature of Gale et al. (2008). In Core SN°4, it is typically represented by the bioturbated surface on top of a prominent limestone bed and overlying organic-rich marlstones.

915 (2) The lithological change towards more carbonate rich and clay/organic lean
916 rocks at the base of Subunit 1c in Core SN°4 corresponds to an abrupt change
917 from organic rich to carbonate rich deposits at ~207 m in Core S13, which was
918 previously correlated to sequence boundary Ce4 (Kuhnt et al., 2009). Although
919 there is no sharp boundary in Core SN°4, an initial change in TOC and carbonate
920 content occurs between 139 and 140 m, followed by a second major change
921 (mainly expressed in the carbonate/terrigenous ratio) at the lithological
922 boundary between Subunits 1c and 2a at 126.80 m.
923 (3) The most prominent TS within the Cenomanian sea level record is associated
924 with Ce3 and was previously identified at Folkestone (Anglo-Paris Basin) and
925 Pueblo, Colorado (Gale et al., 2008). At these locations, Ce3 is located at the base
926 of the Thatcher Limestone in the center of the $\delta^{13}C_{org}$ trough between the two
927 peaks of the carbon isotope excursion and coincides with a major sequence
928 boundary, which forms a characteristic intensely bioturbated hard ground. In the
929 Mohammed Plage section, Ce3 is prominently expressed as the boundary
930 between greenish-gray claystones characterized by extremely low TOC and a
931 nodular limestone bundle at the base of the *T. reicheli* zone (Kuhnt et al., 2009).
932 This TS falls within a period of minimal sedimentation rates within the proximal
933 setting of Mohamed Plage (Kuhnt et al., 2009), indicating sediment transport into
934 more distal parts of the Tarfaya Basin.
935 In Core SN°4, Ce3 at 207.3 m is characterized by the intercalation of light,
936 laminated carbonate rich layers with shell debris, indicating bottom current
937 activity, within a sequence of dark marlstones (Fig. 10A). The NGR logging data
938 show an abrupt increase across the TS, corresponding to the facies change to
939 transgressive organic rich shales. Log(Zr/Rb) and Log(Terr10/Ca) exhibit an

940 increase in grain size within the lowstand carbonate layers, followed by a
941 decrease in grain size and higher clay content above the TS.
942 (4) A prominent TS (Ce2.1) defined by higher Log(Zr/Rb) and NGR is located
943 between 222 and 223 m in the uppermost part of the *T. brotzeni* Zone, close to
944 the onset of the MCE (Fig. 10B). This TS is coeval with a first small $\delta^{13}C_{org}$
945 increase prior to the MCE onset and at ~25 m below Ce3.
946 (5) The transgressive surface at the base of the Cenomanian (Ce0) is located at a
947 maximum in Log(Zr/Rb) at 324 m, close to the top of the ACB.
948
949 ***4.7 C/N ratio and stoichiometry of organic matter indicating water column***
950 ***dysoxia/anoxia and paleoproductivity***
951 The C_{org}/N_{total} ratios (Fig. 5B) in Core SN°4 are on average higher by a
952 factor of 5 than the present day Redfield ratio (Redfield, 1942) of 6.6
953 representative for marine phytoplankton or average values of ~5 in organic-
954 carbon-poor sediments (Bouloubassi et al., 1999). Diagenetic effects that would
955 change the signal by a factor of up to 10 are not known today and the unusually
956 high C/N ratios can be assumed to represent original variability (Meyers 1989,
957 2006). Two possible explanations were presented by Meyers (1989, 2006): (1)
958 recycling of organic matter within the water column and uppermost cm of
959 sediments under suboxic or anoxic conditions or (2) input of terrestrial organic
960 material rich in cellulose. Rock Eval data from parallel cores in the Tarfaya Basin
961 showed a predominance of kerogen types I and II with organic matter mainly
962 consisting of alginite and bituminite that indicate a marine origin (Kuhnt et al.,
963 2001), which excludes a terrestrial source for the N-rich organic matter. Van
964 Mooy et al. (2002) concluded that modes of organic matter recycling differed

965 between oxic and anoxic conditions. Suboxic microbial degradation and
966 denitrification in the water column and at the sea floor preferentially
967 disintegrate amino acids rich in N and lead to elevated C/N ratios. In contrast,
968 post-depositional diagenetic processes result in relative enrichment of N in
969 organic matter and lowered C/N ratios (Müller, 1977; Waples and Sloan, 1980).
970 The relative depletion of N in the SN°4 sedimentary rocks, therefore,
971 indicates suboxic or anoxic conditions within the water column or in the
972 sediments during the sedimentation. A link to high productivity related anoxia is
973 supported by increased C/N values in Mediterranean sapropels (Bouloubassi et
974 al., 1999) and by generally increased values during mid-Cretaceous OAEs
975 (Meyers et al., 2006). Twichell et al. (2002) used the C/N-ratio as proxy for
976 elevated productivity on account of the coupling between increased productivity
977 and water column redox state. The signal seems to be linked to the adaptation of
978 heterotrophic organisms to dysoxic or anoxic conditions. Following this
979 approach, periods with drastically increased C/N-ratio in Core SN°4 represent
980 intervals of exceptionally increased productivity, in particular prior and during
981 OAE2. This early increase in primary production may have been restricted to the
982 northwest African shelf, which was subject to wind-driven upwelling since the
983 early Cenomanian.
984 Enrichment of barium preceding and accompanying the initial $\delta^{13}C_{org}$
985 increase of OAE2 in the proximal Mohamed Plage section was interpreted by
986 Mort et al. (2008) as a productivity increase stimulated by enhanced nutrient
987 input from transgressive flooding of low altitude desert areas. Seismic offshore
988 data indicate an open shelf setting for the Late Cretaceous Tarfaya Basin (e.g.
989 Ranke et al., 1982; Patriat and Labails, 2006) rather than a restricted basin. The

global extent of enhanced productivity and water column oxygen depletion is further supported by the occurrence of coeval elevated phosphorus mass accumulation rates in European (Tethys) and North American (Western Interior Seaway) sections (Mort et al., 2007). These authors interpreted the initial peak in phosphorous accumulation as the result of increased productivity preceding globally enhanced organic carbon burial during OAE2.

5. Conclusions

A high-resolution analysis of a 325 m long continuous sedimentary succession recovered in Core SN°4 from the Tarfaya Basin reveals that terrigenous input as well as carbonate and organic carbon production rates were primarily controlled by a longterm transgressive trend from the late Albian to early Turonian. Three positive carbon isotope excursions are identified in the $\delta^{13}C_{org}$ record: OAE2 in the latest Cenomanian, the MCE during the mid-Cenomanian and the ACB. The most prominent Cenomanian transgressive surface separating two third-order eustatic sea level cycles, SB Ce3 (Haq et al., 1987) is identified close to the second peak of the MCE carbon isotope excursion. Sequence boundary Ce3 coincides with a fundamental change in cyclic sedimentation pattern and marks the onset of a longterm trend in increasing carbonate and organic carbon productivity. Low Log(Mn/S) ratios as well as elevated TOC and C/N ratios indicate intense oxygen depletion during OAE2 and the ACB, which we relate to enhanced primary production during these events. Mean sedimentation rates are 4.5–6 cm/kyr for the late Albian to middle

Cenomanian (200–350 m) and 8-9 cm/kyr for the late Cenomanian to early Turonian. Based on EHA analyses of eccentricity and obliquity signals in the NGR wireline logging data and the XRF-scanner derived Log(Zr/Rb), we estimate the duration of the Cenomanian Stage to be 4.8 ±0.2 Myr.

Acknowledgements

We thank Nils Andersen (Leibniz Laboratory for Radiometric Dating and Stable Isotope Research, Kiel) and Michael Joachismki (GeoZentrum Nordbayern, Friedrich-Alexander Universität Erlangen-Nürnberg) for stable isotope measurements, Dieter Garbe-Schönberg and Samuel Müller (Institute of Geosciences, Kiel) for advice with X□ray fluorescence scanning, and Bettina Domeyer (GEOMAR) for technical help with the CHN Analyzer. RWE Dea AG in cooperation with the Office National des Hydrocarbures et des Mines, Morocco, enabled drilling SN°4 in the framework of the Atlantic Margin Integrated Basin Analysis Project. This research was funded by the German Research Council (DFG) in the framework of SFB 754, TP A7. We gratefully acknowledge two anonymous reviewers for comments and suggestions that significantly improved the manuscript.

References:

Ando, A., Huber, B. T., MacLeod, K. G., Ohta, T., Boo-Keun Khim, B.-K., 2009. Blake Nose stable isotopic evidence against the mid-Cenomanian glaciation hypothesis. Geology, 37, 451-454. http://dx.doi.org/10.1130/G25580A.1.

Aquit, M., Kuhnt, W., Holbourn, A., Chellai, E. H., Stattegger, K., Kluth, O., Jabour, H., 2013. Late Cretaceous paleoenvironmental evolution of the Tarfaya Atlantic coastal basin, SW Morocco. Cretaceous Research, 45, 288-305. http://dx.doi.org/10.1016/j.cretres.2013.05.004.

Aquit, M., Kuhnt, W., Holbourn, A. E., Chellai, E. H., Lees, J. A., Kluth, O., Jabour, H., 2016. Complete archive of middle Turonian to early Campanian sedimentary deposition in newly drilled cores from the Tarfaya Basin, SW Morocco. Geological Society of America Bulletin, B31523.1. http://dx.doi.org/10.1130/B31523.1.

Barclay, R. S., McElwain, J. C., Sageman, B. B., 2010. Carbon sequestration activated by a volcanic CO2 pulse during Ocean Anoxic Event 2. Nature Geoscience, 3(3), 205-208. http://dx.doi.org/10.1038/ngeo757.

Barker, I. R., Moser, D. E., Kamo, S. L., Plint, A. G., 2011. High-precision U–Pb zircon ID–TIMS dating of two regionally extensive bentonites: Cenomanian Stage, Western Canada Foreland Basin. Canadian Journal of Earth Sciences, 48(2), 543-556. http://dx.doi.org/10.1139/E10-042.

Berger, A. L., Loutre, M. F., Laskar, J., 1992. Stability of the astronomical frequencies over the Earth's history for paleoclimate studies. Science, *255*(5044), 560. http://dx.doi.org/10.1126/science.255.5044.560.

Bouloubassi, I., Rullkötter, J., Meyers, P. A., 1999. Origin and transformation of organic matter in Pliocene–Pleistocene Mediterranean sapropels: organic geochemical evidence

reviewed. Marine Geology, 153(1), 177-197. http://dx.doi.org/10.1016/S0025-3227(98)00082-6.

Boulila, S., Galbrun, B., Miller, K. G., Pekar, S. F., Browning, J. V., Laskar, J., Wright, J. D., 2011. On the origin of Cenozoic and Mesozoic "third-order" eustatic sequences. Earth-Science Reviews, *109*(3), 94-112. http://dx.doi.org/10.1016/j.earscirev.2011.09.003.

Bruland, K. W., 1983. Trace elements in the sea. Chemical Oceanography, *8*.

Brumsack, H. J., 2006. The trace metal content of recent organic carbon-rich sediments: implications for Cretaceous black shale formation. Palaeogeography, Palaeoclimatology, Palaeoecology, *232*(2), 344-361. http://dx.doi.org/10.1016/j.palaeo.2005.05.011.

Calvert, S. E., Pedersen, T. F., 2007. Chapter fourteen elemental proxies for palaeoclimatic and palaeoceanographic variability in marine sediments: interpretation and application. Developments in Marine Geology, 1, 567-644. http://dx.doi.org/10.1016/S1572-5480(07)01019-6.

Clarke, L. J., Jenkyns, H. C., 1999. New oxygen isotope evidence for long-term Cretaceous climatic change in the Southern Hemisphere. Geology, 27(8), 699–702. http://dx.doi.org/10.1130/0091-7613(1999)027<0699:NOIEFL>2.3.CO;2.

Coccioni, R., Galeotti, S., 2003. The mid-Cenomanian Event: prelude to OAE 2. Palaeogeography, Palaeoclimatology, Palaeoecology 190, 427-440. http://dx.doi.org/10.1016/S0031-0182(02)00617-X.

Du Vivier, David Selby, D. S., Sageman, B. B., Jarvis, I., Gröcke, D. R., Voigt, S., 2014. Marine 187Os/188Os isotope stratigraphy reveals the interaction of volcanism and ocean circulation during Oceanic Anoxic Event 2. Earth and Planetary Science Letters, 389, 23-33. http://dx.doi.org/10.1016/j.epsl.2013.12.024.

Flögel, S., Wallmann, K., Poulsen, C. J., Zhou, J., Oschlies, A., Voigt, S., Kuhnt, W., 2011. Simulating the biogeochemical effects of volcanic CO2 degassing on the oxygen-state of the deep ocean during the Cenomanian/Turonian Anoxic Event (OAE2). Earth and Planetary Science Letters, 305(3–4), 371-384. http://dx.doi.org/10.1016/j.epsl.2011.03.018.

Forster, A., Schouten, S., Baas, M., Damsté, J. S. S., 2007. Mid-Cretaceous (Albian–Santonian) sea surface temperature record of the tropical Atlantic Ocean. Geology, 35(10), 919-922. http://dx.doi.org/10.1130/G23874A.1.

Gale, A. S., Jenkyns, H. C., Kennedy, W. J., Corfield, R. M., 1993. Chemostratigraphy versus biostratigraphy: data from around the Cenomanian–Turonian boundary. Journal of the Geological Society, 15*0*(1), 29-32. http://dx.doi.org/10.1144/gsjgs.150.1.0029.

Gale, A. S., Young, J. R., Shackleton, N. J., Crowhurst, S. J., Wray, D. S., 1999. Orbital tuning of Cenomanian marly chalk successions: towards a Milankovitch time-scale for the Late Cretaceous. Philosophical Transactions of the Royal Society of London A: Mathematical, Physical and Engineering Sciences, 357(1757), 1815-1829. http://dx.doi.org/10.1098/rsta.1999.0402

Gale, A. S., Hardenbol, J., Hathway, B., Kennedy, W. J., Young, J. R., Phansalkar, V., 2002. Global correlation of Cenomanian (Upper Cretaceous) sequences: Evidence for Milankovitch control on sea level. Geology, 30(4), 291-294. http://dx.doi.org/10.1130/0091-7613(2002)030%3C0291:GCOCUC%3E2.0.CO;2.

Gale, A. S., 2007. A Milankovitch scale for the Cenomanian. Terra Nova 1, 420-425.

Gale, A. S., Voigt, S., Sageman, B. B., Kennedy, W. J., 2008. Eustatic sea-level record for the Cenomanian (Late Cretaceous) - extension to the Western Interior Basin, USA. Geology, 36(11), 859-862. http://dx.doi.org/10.1130/G24838A.1.

Giraud, F., Reboulet, S., Deconinck, J. F., Martinez, M., Carpentier, A. Bréziat, C., 2013. The Mid-Cenomanian Event in southeastern France: Evidence from palaeontological and clay mineralogical data. Cretaceous Research 46, 43-58. http://dx.doi.org/10.1016/j.cretres.2013.09.004.

Govin, A., Holzwarth, U., Heslop, D., Ford Keeling, L., Zabel, M., Mulitza, S., Collins, J. A., Chiessi, C. M., 2012. Distribution of major elements in Atlantic surface sediments (36 N–49 S): Imprint of terrigenous input and continental weathering. Geochemistry, Geophysics, Geosystems, 13(1), Q01013. http://dx.doi.org/10.1029/2011GC003785.

Gradstein, F. M., Ogg, J. G., Schmitz, M., Ogg, G. (Eds.), 2012. *The geologic time scale 2012*. elsevier. http://dx.doi.org/10.1016/c2011-1-08249-8.

Hardas, P., Mutterlose, J., Friedrich, O., Erbacher, J., 2012. The Middle Cenomanian Event in the equatorial Atlantic: The calcareous nannofossil and benthic foraminiferal response. Marine Micropaleontology 96–97, 66–74. http://dx.doi.org/10.1016/j.marmicro.2012.08.003.

Haq, B. U., Hardenbol, J., Vail, P. R., 1987. Chronology of fluctuating sea levels since the Triassic. Science, 235(4793), 1156-1167. http://dx.doi.org/10.1126/science.235.4793.1156.

Haq, B. U., 2014. Cretaceous eustasy revisited. Global and Planetary Change, 113, 44-58. http://dx.doi.org/10.1016/j.gloplacha.2013.12.007.

Holbourn, A., Kuhnt, W., El Albani, A., Pletsch, T., Luderer, F., Wagner, T., 1999. Upper Cretaceous palaeoenvironments and benthonic foraminiferal assemblages of potential source rocks from the western African margin, Central Atlantic. Geological Society, London, Special Publications, 153(1), 195-222. http://dx.doi.org/10.1144/GSL.SP.1999.153.01.13.

Jarvis, I., Murphy, A. M., Gale, A. S., 2001. Geochemistry of pelagic and hemipelagic carbonates: criteria for identifying systems tracts and sea-level change. Journal of the Geological Society, London 158, 685-696. http://dx.doi.org/10.1144/jgs.158.4.685.

Jarvis, I. A. N., Gale, A. S., Jenkyns, H. C., Pearce, M. A., 2006. Secular variation in Late Cretaceous carbon isotopes: a new δ 13 C carbonate reference curve for the Cenomanian–Campanian (99.6–70.6 Ma). Geological Magazine, 143(05), 561-608. http://dx.doi.org/10.1017/S0016756806002421.

Jarvis, I., Lignum, J. S., Gröcke, D. R., Jenkyns, H. C., Pearce, M. A., 2011. Black shale deposition, atmospheric CO2 drawdown, and cooling during the Cenomanian□Turonian Oceanic Anoxic Event. Paleoceanography, 26(3), PA3201. http://dx.doi.org/10.1029/2010PA002081.

Kolonic, S., Wagner, T., Forster, A., Sinninghe Damsté, J.S., Walsworth-Bell, B., Erba, E., Turgeon, S., Brumsack, H.J., Chellai, E.H., Tsikos, H., Kuhnt, W., and Kuypers, M.M.M., 2005. Black shale deposition on the northwest African Shelf during the Cenomanian/Turonian oceanic anoxic event: Climate coupling and global organic carbon burial: Paleoceanography, 20, 1–18. http://doi.org/10.1029/2003PA000950.

Kuhnt, W., Herbin, J. P., Thurow, J., Wiedmann, J., 1990. Distribution of Cenomanian-Turonian organic facies in the western Mediterranean and along the adjacent Atlantic margin. In: Huc, A. Y. (Ed.), Deposition of organic facies (Vol. 30). AAPG, Tulsa, 133-160.

Kuhnt, W., Nederbragt, A., Leine, L., 1997. Cyclicity of Cenomanian-Turonian organic-carbon-rich sediments in the Tarfaya Atlantic coastal basin (Morocco). Cretaceous Research, 18(4), 587-601. https://doi.org/10.1006/cres.1997.0076.

Kuhnt, W., Chellai, E. H., Holbourn, A., Luderer, F., Thurow, J., Wagner, T., El Albani, A., Beckmann, B., Herbin, J.-P., Kawamura, H., Kolonic, S., 2001. Morocco Basin's sedimentary

record may provide correlations for Cretaceous paleoceanographic events worldwide. Eos, Transactions American Geophysical Union, 82(33), 361-364. http://dx.doi.org/10.1029/01EO00223.

Kuhnt, W., Luderer, F., Nederbragt, S., Thurow, J., Wagner, T., 2005. Orbital-scale record of the late Cenomanian–Turonian oceanic anoxic event (OAE-2) in the Tarfaya Basin (Morocco). International Journal of Earth Sciences, 94(1), 147-159. http://dx.doi.org/10.1007/s00531-004-0440-5.

Kuhnt, W., Holbourn, A., Gale, A., Chellai, E. H., Kennedy, W. J., 2009. Cenomanian sequence stratigraphy and sea-level fluctuations in the Tarfaya Basin (SW Morocco). Geological Society of America Bulletin, 121(11-12), 1695-1710. http://dx.doi.org/10.1130/B26418.1.

Kuhnt, W., Holbourn, A. E., Beil, S., Aquit, M., Krawczyk, T., Flögel, S., Chellai, E. H., Jabour, H., 2017. Unraveling the onset of Cretaceous Oceanic Anoxic Event 2 in an extended sediment archive from the Tarfaya-Laayoune Basin, Morocco. Paleoceanography, 32, 923–946. http://dx.doi.org/10.1002/2017PA003146.

Landing, W. M., Bruland, K. W., 1980. Manganese in the north Pacific. Earth and Planetary Science Letters, 49(1), 45-56. http://dx.doi.org/10.1016/0012-821X(80)90149-1.

Laskar, J., Robutel, P., Joutel, F., Gastineau, M., Correia, A. C. M., Levrard, B., 2004. A long-term numerical solution for the insolation quantities of the Earth. Astronomy & Astrophysics, 428(1), 261-285. http://dx.doi.org/10.1051/0004-6361:20041335.

Laskar, J., Fienga, A., Gastineau, M., Manche, H., 2011a. La2010: a new orbital solution for the long-term motion of the Earth. Astronomy & Astrophysics, 532, A89. http://dx.doi.org/10.1051/0004-6361/201116836.

1219 Laskar, J., Gastineau, M., Delisle, J. B., Farrés, A., Fienga, A., 2011b. Strong chaos induced
1220 by close encounters with Ceres and Vesta. Astronomy & Astrophysics, *532*, L4.
1221 http://dx.doi.org/10.1051/0004-6361/201117504.
1222
1223 Laurin, J., Meyers, S. R., Uličný, D., Jarvis, I., Sageman, B. B., 2015. Axial obliquity control on
1224 the greenhouse carbon budget through middle- to high-latitude reservoirs. Paleoceanography,
1225 30, 133–149. http://dx.doi.org/10.1002/2014PA002736.
1226
1227 Leine, L. 1986. Geology of the Tarfaya oil shale deposit, Morocco. Geologic en Mijnbouw, 65,
1228 57-74.
1229
1230 Lhomme, N., Clarke, G. K. C., Ritz, C., 2005. Global budget of water isotopes inferred from
1231 polar ice sheets. Geophysical Research Letters, 32, L20502,
1232 http://dx.doi.org/10.1029/2005GL023774.
1233
1234 Mann, M. E., Lees, J. M., 1996. Robust estimation of background noise and signal detection
1235 in climatic time series. Climatic Change, 33(3), 409-445.
1236 http://dx.doi.org/10.1007/BF00142586.
1237
1238 Meissner, K. J., McNeil, B. I., Eby, M., Wiebe, E. C., 2012. The importance of the terrestrial
1239 weathering feedback for multimillennial coral reef habitat recovery. Global Biogeochemical
1240 Cycles, 26, GB3017. http://dx.doi.org/ 10.1029/2011GB004098.
1241
1242 Meyers, P. A., 1989. Sources and deposition of organic matter in Cretaceous passive margin
1243 deep-sea sediments: a synthesis of organic geochemical studies from Deep Sea Drilling
1244 Project Site 603, outer Hatteras Rise. Marine and petroleum geology, 6(2), 182-189.
1245 http://dx.doi.org/10.1016/0264-8172(89)90021-4.
1246

1247 Meyers, P. A., 2006. Paleoceanographic and paleoclimatic similarities between
1248 Mediterranean sapropels and Cretaceous black shales. Palaeogeography, Palaeoclimatology,
1249 Palaeoecology, 235(1), 305-320. http://dx.doi.org/10.1016/j.palaeo.2005.10.025.
1250
1251 Meyers, P. A., Bernasconi, S. M., Forster, A., 2006. Origins and accumulation of organic
1252 matter in expanded Albian to Santonian black shale sequences on the Demerara Rise, South
1253 American margin. Organic Geochemistry, 37(12), 1816-1830.
1254 http://dx.doi.org/10.1016/j.orggeochem.2006.08.009.
1255
1256 Meyers, S. R., Sageman, B. B., 2007. Quantification of deep-time orbital forcing by average
1257 spectral misfit. American Journal of Science, 307(5), 773-792.
1258 http://dx.doi.org/10.2475/05.2007.01.
1259
1260 Meyers, S. R., Sageman, B. B., Arthur, M. A., 2012. Obliquity forcing of organic matter
1261 accumulation during Oceanic Anoxic Event 2. Paleoceanography, 27(3).
1262 http://dx.doi.org/10.1029/2012PA002286.
1263
1264 Miller, K. G., Sugarman, P. J., Browning, J. V., Kominz, M. A., Hernández, J. C., Olsson, R. K.,
1265 Wright, J. D., Feigenson, M. D., Van Sickel, W., 2003. Late Cretaceous chronology of large,
1266 rapid sea-level changes: Glacioeustasy during the greenhouse world. Geology, 31, 585–588.
1267 http://dx.doi.org/10.1130/0091-7613(2003)031%3C0585:LCCOLR%3E2.0.CO;2.
1268
1269 Miller, K. G., Wright, J. D., Browning, J. V. 2005. Visions of ice sheets in a greenhouse world.
1270 Marine Geology, 217, 215–231. http://dx.doi.org/10.1016/j.margeo.2005.02.007.
1271
1272 Mitchell, S. F., Paul, C. R. C., Gale A. S., 1996. Carbon isotopes and sequence Stratigraphy.
1273 In Howell, J.A., Aitken, J.F. (Eds.), High Resolution Sequence Stratigraphy: Innovations and
1274 Applications. Geological Society, London, Special Publications 104, 11-24.
1275 http://dx.doi.org/10.1144/GSL.SP.1996.104.01.02.
1276

1277 Mitchell, S. F., Carr, I. T., 1998. Foraminifera response to mid-Cenomanian (Upper
1278 Cretaceous) palaeoceanographic events in the Anglo-Paris Basin (Northwest Europe).
1279 Palaeogeography, Palaeoceanography, Palaeoecology 137, 103-125.
1280 http://dx.doi.org/10.1016/S0031-0182(97)00087-4.
1281
1282 Moriya, K., Wilson, P. A., Friedrich, O., Erbacher, J., Kawahata, H., 2007. Testing for ice
1283 sheets during the mid-Cretaceous greenhouse using glassy foraminiferal calcite from the mid-
1284 Cenomanian tropics on Demerara Rise. Geology, 35, 615–618.
1285 http://dx.doi.org/10.1130/G23589A.1.
1286
1287 Mort, H. P., Adatte, T., Föllmi, K. B., Keller, G., Steinmann, P., Matera, V., Berner, Z., Stüben,
1288 D., 2007. Phosphorus and the roles of productivity and nutrient recycling during oceanic
1289 anoxic event 2. Geology, 35(6), 483–486. https://dx.doi.org/10.1130/G23475A.1.
1290
1291 Mort, H. P., Adatte, T., Keller, G., Bartels, D., Föllmi, K. B., Steinmann, P., Berner, Z., Chellai,
1292 E. H., 2008. Organic carbon deposition and phosphorus accumulation during Oceanic Anoxic
1293 Event 2 in Tarfaya, Morocco. Cretaceous Research, 29(5–6), 1008-1023.
1294 https://dx.doi.org/10.1016/j.cretres.2008.05.026.
1295
1296 Mulitza, S., Prange, M., Stuut, J. B., Zabel, M., von Dobeneck, T., Itambi, A. C., Nizou, J.,
1297 Schulz, M., Wefer, G., 2008. Sahel megadroughts triggered by glacial slowdowns of Atlantic
1298 meridional overturning. Paleoceanography, *23*(4), PA4206.
1299 http://dx.doi.org/10.1029/2008PA001637.
1300
1301 Müller, P. J., 1977. CN ratios in Pacific deep-sea sediments: Effect of inorganic ammonium
1302 and organic nitrogen compounds sorbed by clays. Geochimica et Cosmochimica Acta, 41(6),
1303 765-776. http://dx.doi.org/10.1016/0016-7037(77)90047-3.
1304
1305 Nelson, C.S., Smith, A.M., 1996. Stable oxygen and carbon isotope compositional fields for
1306 skeletal and diagenetic components in New Zealand Cenozoic nontropical carbonate

1307 sediments and limestones: A synthesis and review. New Zealand Journal of Geology and
1308 Geophysics, 39(1), 93–107. http://dx.doi.org/10.1080/00288306.1996.9514697
1309
1310 Niebuhr, B., 2005. Geochemistry and time-series analyses of orbitally forced Upper
1311 Cretaceous marl–limestone rhythmites (Lehrte West Syncline, northern Germany). Geological
1312 Magazine, *142*(01), 31-55. http://dx.doi.org/10.1017/S0016756804009999.
1313
1314 Obradovitch, J. D., 1993, A Cretaceous time scale. In: Caldwell, W. G. E., Kauffman, E. G.,
1315 (Ed.), Evolution of the Western Interior basin: Geological Association of Canada Special
1316 Paper 39, 379–396.
1317
1318 Patriat, M., Labails, C., (2006). Linking the Canary and Cape-Verde Hot-Spots, Northwest
1319 Africa. Marine Geophysical Researches, 27(3), 201-215. http://dx.doi.org/10.1007/s11001-
1320 006-9000-7,
1321
1322 Patterson, M. O., McKay, R., Naish, T., Escutia, C., Jimenez-Espejo, F. J., Raymo, M. E.,
1323 Meyers, S. R., Tauxe, L., Brinkhuis, H., IODP Expedition 318 Scientists, 2014. Orbital forcing
1324 of the East Antarctic ice sheet during the Pliocene and Early Pleistocene. Nature
1325 Geoscience, 7(11), 841-847. http://dx.doi.org/10.1038/ngeo2273.
1326
1327 Paul, C. R. C., Mitchell, S. F., Marshall, J. D., Leary, P. N., Gale, A. S., Duane, A. M,
1328 Ditchfield, P. W., 1994. Palaeoceanographic events in the middle Cenomanian of Northwest
1329 Europe. Cretaceous Research 15, 707-738. http://dx.doi.org/10.1006/cres.1994.1039.
1330
1331 Pearce, M. A., Jarvis, I., Tocher, B. A., 2009. The Cenomanian–Turonian boundary event,
1332 OAE2 and palaeoenvironmental change in epicontinental seas: New insights from the
1333 dinocyst and geochemical records. Palaeogeography, Palaeoclimatology,
1334 Palaeoecology, 2*80*(1), 207-234. http://dx.doi.org/10.1016/j.palaeo.2009.06.012.
1335

1336 Peterson, L. C., Haug, G. H., Hughen, K. A., Röhl, U., 2000. Rapid changes in the hydrologic
1337 cycle of the tropical Atlantic during the last glacial. Science, 290(5498), 1947-1951.
1338 http://dx.doi.org/10.1126/science.290.5498.1947.
1339
1340 Petrizzo, M., Caron, M., Premoli Silva, I., 2015. Remarks on the identification of the
1341 Albian/Cenomanian boundary and taxonomic clarification of the planktonic foraminifera index
1342 species globotruncanoides, brotzeni and tehamaensis. Geological Magazine, 152(3), 521-536.
1343 http://dx.doi.org/10.1017/S0016756814000478.
1344
1345 R Core Team, 2017. R: A language and environment for statistical computing. R Foundation
1346 for Statistical Computing, Vienna, Austria. URL https://www.R-project.org/.
1347
1348 Rachold, V., Brumsack, H. J., 2001. Inorganic geochemistry of Albian sediments from the
1349 Lower Saxony Basin NW Germany: palaeoenvironmental constraints and orbital
1350 cycles. Palaeogeography, Palaeoclimatology, Palaeoecology, 174(1), 121-143.
1351 http://dx.doi.org/10.1016/S0031-0182(01)00290-5.
1352
1353 Ranke, U., von Rad, U., Wissmann, G., 1982. Stratigraphy, Facies and Tectonic Development
1354 of the On- and Offshore Aaiun-Tarfaya Basin - A Review. In: von Rad, U., K. Hinz, Sarnthein,
1355 M., Seibold, E. (Eds.), Geology of the Northwest African Continental Margin. Springer, Berlin,
1356 Heidelberg, 86–105. http://dx.doi.org/10.1007/978-3-642-68409-8_6
1357
1358 Redfield, A. C., 1942. The processes determining the concentration of oxygen, phosphate
1359 and other organic derivatives within the depths of the Atlantic Ocean. Massachusetts Institute
1360 of Technology and Woods Hole Oceanographic Institution.
1361 http://dx.doi.org/10.1575/1912/1053.
1362
1363 Robaszynski, F., Caron, M., 1995. Foraminifères planctoniques du Crétacé; commentaire de
1364 la zonation Europe-Méditerranée. Bulletin de la Société géologique de France, 166(6), 681-
1365 692.

Scott, R. W., Oboh-Ikuenobe, F. E., Benson Jr, D. G., Holbrook, J. M., 2009. Numerical age calibration of the Albian/Cenomanian boundary. Stratigraphy, 6(1), 17-32.

Scott, R. W., 2014. A Cretaceous chronostratigraphic database: construction and applications. Carnets de Geologie-Notebooks on Geology, 14(2), 15-37. http://dx.doi.org/10.4267/2042/53522.

Stoll, H. M., Schrag, D. P., 2000, High-resolution stable isotope records from the Upper Cretaceous rocks of Italy and Spain: Glacial episodes in a greenhouse planet?. Geological Society of America Bulletin, 112, 308–319. http://dx.doi.org/10.1130/0016-7606(2000)112%3C308:HSIRFT%3E2.0.CO;2.

Tisserand, A., Malaizé, B., Jullien, E., Zaragosi, S., Charlier, K., Grousset, F., 2009. African monsoon enhancement during the penultimate glacial period (MIS 6.5□170 ka) and its atmospheric impact. Paleoceanography, 24(2), PA2220. http://dx.doi.org/10.1029/2008PA001630.

Torrence, C., Compo, G. P., 1998. A practical guide to wavelet analysis. Bulletin of the American Meteorological Society. 79, 61-78. http://dx.doi.org/10.1175/1520-0477(1998)079%3C0061:APGTWA%3E2.0.CO;2

Tsikos, H., Jenkyns, H. C., Walsworth-Bell, B., Petrizzo, M. R., Forster, A., Kolonic, S., Erba, E., Premoli Silva, I., Baas, M., Wagner, T., Sinninghe Damsté, J. S., 2004. Carbon-isotope stratigraphy recorded by the Cenomanian-Turonian Oceanic Anoxic Event: Correlation and implications based on three key localities. Journal of the Geological Society, 161, 711–719. http://dx.doi.org/10.1144/0016-764903-077.

Turgeon, S. C., Ceaser, R. A., 2008. Cretaceous oceanic anoxic event 2 triggered by a massive magmatic episode. Nature, 454, 323–326. http://dx.doi.org/10.1038/nature07076.

Twichell, S. C., Meyers, P. A., Diester-Haass, L., 2002. Significance of high C/N ratios in organic-carbon-rich Neogene sediments under the Benguela Current upwelling system. Organic Geochemistry, *33*(7), 715-722. http://dx.doi.org/10.1016/S0146-6380(02)00042-6.

Van Mooy, B. A., Keil, R. G., Devol, A. H., 2002. Impact of suboxia on sinking particulate organic carbon: Enhanced carbon flux and preferential degradation of amino acids via denitrification. Geochimica et Cosmochimica Acta, *66*(3), 457-465. http://dx.doi.org/10.1016/S0016-7037(01)00787-6.

Voigt, S., Hilbrecht, H., 1997. Late Cretaceous carbon isotope stratigraphy in Europe: Correlation and relations with sea level and sediment stability. Palaeogeography, Palaeoclimatology, Palaeoecology, 134(1–4), 39-59. http://dx.doi.org/10.1016/S0031-0182(96)00156-3.

Voigt, S., Gale, A. S., and Flögel, S., 2004. Midlatitude shelf seas in the Cenomanian-Turonian greenhouse world: Temperature evolution and North Atlantic circulation. Paleoceanography, 19, PA4020, http://dx.doi.org/10.1029/2004PA001015.

Waples, D. W., & Sloan, J. R., 1980. Carbon and nitrogen diagenesis in deep sea sediments. Geochimica et Cosmochimica Acta, 44(10), 1463-1470. http://dx.doi.org/10.1016/0016-7037(80)90111-8.

Weaver, C. E., 1967. Potassium, illite and the ocean. Geochimica et Cosmochimica Acta, *31*(11), 2181-2196. http://dx.doi.org/10.1016/0016-7037(67)90060-9.

Weaver, C. E., 1989. Clays, muds, and shales (Vol. 44). Elsevier.

1425 Weaver, A. J., Eby, M., Wiebe, E. C., Bitz, C. M., Duffy, P. B., Ewen, T. L., Fanning, A. F.,
1426 Holland, M. M., MacFadyen, A., Matthews, H. D., Meissner, K. J., Saenko, O., Schmittner, A.,
1427 Wang, H., Yoshimori, M., 2001 The UVic earth system climate model: Model description,
1428 climatology, and applications to past, present and future climates. Atmosphere-Ocean, 39, 4.
1429 http://dx.doi.org/10.1080/07055900.2001.9649686.
1430
1431 Weltje, G. J., Tjallingii, R., 2008. Calibration of XRF core scanners for quantitative
1432 geochemical logging of sediment cores: theory and application. Earth and Planetary Science
1433 Letters, 274(3), 423-438. http://dx.doi.org/10.1016/j.epsl.2008.07.054.
1434
1435 Wilson, P. A., Norris, R. D., Cooper, M. J., 2002. Testing the Cretaceous greenhouse
1436 hypothesis using glassy foraminiferal calcite from the core of the Turonian tropics on
1437 Demerara Rise. Geology, 30(7), 607–610. http://dx.doi.org/10.1130/0091-
1438 7613(2002)030<0607:TTCGHU>2.0.CO;2
1439
1440
1441
1442

1443 ***Figure 1*:** Location of Tarfaya Basin within the modeled "hotspot" of Late Cetaceous tropical
1444 anoxia. Oxygen concentration (mol/m^3) in 300 m water depth, calculated with the University of
1445 Victoria (UVic) Intermediate Complexity Earth System Climate Model (Weaver et al., 2001) with
1446 500 ppm pCO_2 and Cenomanian/Turonian boundary conditions.
1447
1448 ***Figure 2:*** Location of coring site SN°4 in relation to Shell/ONAREP Cores S13, S57, S75 and the
1449 outcrop section at "Mohamed Plage" (modified from Aquit et al., 2016)
1450
1451 ***Figure 3*:** Natural Gamma Ray logging record of Core SN°4. **A.** Complete record with smooth
1452 interpolation using a Stineman function, numbers refer to lithological subunits. **B.** Upper 125 m
1453 of NGR analyzed with wavelet power spectrum, numbers refer to sedimentary cycles following
1454 the numbering scheme of Kuhnt et al. (1997). **C.** Wavelet spectrum of NGR calculated following
1455 Torrence and Compo (1998), using the software available at URL:
1456 http://atoc.colorado.edu/research/wavelets. Main periodicities referring to long eccentricity
1457 (405 kyr) and obliquity (38 kyr) are marked with black dotted lines, estimated sedimentation
1458 rates fluctuate at ~6-7 cm/kyr for the part below 84 m and at ~8-9 cm/kyr above 84 m. Note the
1459 decrease in spectral power below ~120 m core depth.
1460
1461 ***Figure 4A:*** Lithology, biostratigraphy and chronostratigraphy of Core SN°4
1462
1463 ***Figure 4B:*** Lithological boundaries between subunits in Core SN°4. Number in red indicates
1464 depth of lithological boundary. Section and segment number are given below each photo.
1465
1466 ***Figure 5A:*** Paleoenvironmental proxy records from Core SN°4: **A.** carbonate content (%), **B.**
1467 XRF-derived Log(Terr10Ca) interpreted as proxy for terrigenous input, **C.** XRF-derived
1468 Log(Zr/Rb) interpreted as grain size variability, **D.** XRF-derived Log(K/Al) representative of
1469 variations of the clay mineral assemblage and **E.** XRF-derived Log(Mn/S) interpreted as redox-
1470 proxy for water column conditions. Column at the top represents lithology, chrono- and
1471 biostratigraphy.
1472

1473 ***Figure 5B:*** Paleoenvironmental proxy records from Core SN°4: **A.** TOC (%), **B.** C_{org}/N_{total}-ratio
1474 measured on bulk material, **C.** $\delta^{13}C_{org}$, **D.** $\delta^{13}C_{carbonate}$ and **E.** $\delta^{18}O$. Column at the top represents
1475 lithology, chrono- and biostratigraphy.
1476
1477 ***Figure 6:*** Frequency analysis of Natural Gamma Ray (NGR) from SN°4 bore hole log data. **A.** NGR
1478 dataset. **B.** $\delta^{13}C_{org}$, **C**. EHA, **D.** mtmML96 power spectrum of NGR over depth interval 60 to 110 m
1479 highlighted in turquoise encompassing OAE2 calculated with Astrochron (Meyers et al., 2012).
1480 For interpretation of marked peaks in power spectrum see Table 1.
1481
1482 ***Figure 7:*** Frequency analysis of XRF scanner derived proxy data. **A.** Log(Zr/Rb) time series. **B.**
1483 $\delta^{13}C_{org}$, **C**. EHA calculated over entire core. **D.** mtmML96 power spectrum of Log(Zr/Rb)
1484 calculated over interval 200 to 350 m highlighted in turquoise with Astrochron (Meyers et al.,
1485 2012). Dotted lines in power spectrum indicate 90, 95 and 99% confidence intervals. For
1486 interpretation of marked peaks in spectrum see Table 2.
1487
1488 ***Figure 8:*** Examples for potential orbital configurations during late Albian to early Turonian from
1489 Laskar et al. (2004 (**A**, **B**), 2011a (**C**) and 2011b (**B**)). Due to the chaotic behavior of the inner
1490 solar system, power spectra of the displayed curves can only be used to extract wavelengths for
1491 the main periodicities of **D** eccentricity (405.49 (E1), 127.14 (E2), and 96.79 kyr (E3)), **E**
1492 obliquity (48.24 (O1) and 37.64 kyr (O2)) and **F** precession (22.46 (P1) and 18.33 kyr (P2)).
1493
1494 ***Figure 9*****:** Sea level influenced paleoenvironmental proxies from Core SN°4: **A.** carbonate content
1495 (%), **B.** XRF-derived Log(Terr10/Ca) interpreted as proxy for terrigenous input, **C.** XRF-derived
1496 Log(Zr/Rb) interpreted as grain size variability, **D.** NGR (cps) and **E.** TOC (%). Vertical lines mark
1497 transgressive surfaces with corresponding sequences after Gale et al., (2002).
1498
1499 ***Figure 10A:*** Facies change across Ce2.1 and Ce3 in Core SN°4. **D.** Nodular carbonate beds with
1500 overlying coarse flaser-laminated marlstones correspond to Ce2.1. **B.** Organic-rich black shales
1501 with increased clay mineral content correspond to Ce3. Laminated carbonate rich intervals with
1502 small-scale erosional base indicate current redeposition (Ce3). Black shale deposition indicates a

1503 subsidence-related deeper environmental setting during Ce3 than during Ce2.1. Sequence
1504 boundaries (SB) are marked in red, the transgressive surface of Ce2.1 in blue.
1505
1506 ***Figure 10B*****:** Transgressive surfaces (TS) correlative to Ce2.1 and Ce3 in Core SN°4. Note
1507 increases in Log(Zr/Rb) below TS and distinct increases in NGR at TS. Ce2.1 and Ce3 are
1508 associated with global $\delta^{13}C$ increases. Blue shading marks sea level lowstands. Dotted lines mark
1509 TS. Yellow shading marks MCE interval. **A.** NGR in cps. **B.** XRF-derived Log(Terr10/Ca)
1510 interpreted as proxy for terrigenous input. **C.** XRF-derived Log(Zr/Rb) interpreted as grain size
1511 variability. **D.** $\delta^{13}C_{org.}$ and $\delta^{13}C_{carbonate}$ **E.** $\delta^{18}O$.
1512
1513 ***Table 1***: Comparison of detected frequencies in Core SN°4 NGR (60 – 110 m) and orbital cycles
1514 from orbital solutions La04 (Laskar et al., 2004), La10 (Laskar et al., 2011a) and La11 (Laskar et
1515 al., 2011b). Orbital terms in brackets denote statistically not significant frequencies (CL<90%).
1516 E1: long eccentricity, E2, E3: short eccentricity, O1, O2: obliquity and P1, P2: precession.
1517
1518 ***Table 2***: Detected frequencies of Log(Zr/Rb) in Core SN°4 (200 – 350 m) and orbital cycles
1519 extracted from orbital solutions La04 (Laskar et al., 2004), La10 (Laskar et al., 2011a) and La11
1520 (Laskar et al, 2011b). E1: long eccentricity, E2, E3: short eccentricity, O1, O2: obliquity and P1,
1521 P2: precession.
1522

Table 1

NGR in SN℄4 (60–110 m)				Extracted frequencies from Laskar et al. (2004, 2011a, 2011b)		
Frequency (cycles/m)	Wave-length (m)	Confidence level (%)	Ratio	Orbital term	Wave-length (kyr)	Ratio
0.031923 (0.025-0.039)	31.33	>90	1	E1	405.49	1
0.14765 (0.139-0.172)	6.77		0.22	(E3)	96.79	0.24
0.24741 (0.240-0.259)	4.04	>95	0.13	O1	48.24	0.12
0.33121 (0.320-0.335)	3.02		0.10	(O2)	37.64	0.09
0.47087 (0.462-0.479)	2.12	>90	0.07	P1	22.46	0.06
0.70231 (0.690-0.710)	1.42		0.05	(P2)	18.33	0.05

Table 2

Log(Zr/Rb) in SN℁4 (200–350 m)				Extracted frequencie s from Laskar et al. (2004, 2011a, 2011b)		
Frequency (cycles/m)	Wave-length (m)	Confidence level (%)	Ratio	Orbital term	Wave-length (kyr)	Ratio
0.02130 (0.011-0.031)	46.96	>99				
0.04658 (0.044-0.048)	21.47	>95		E1	405.49	1
0.06921 (0.059-0.071)	14.45	>90		E1	405.49	1
0.10914 (0.106-0.116)	9.16	>90		heterodyne E2/3-E1		
0.19032 (0.171-0.215)	5.25			E2+E3	127.14 96.79	0.31 0.24
0.31809 (0.305-0.321)	3.14			O1	48.24	0.12
0.62686 (0.602-0.640)	1.60			O2	37.64	

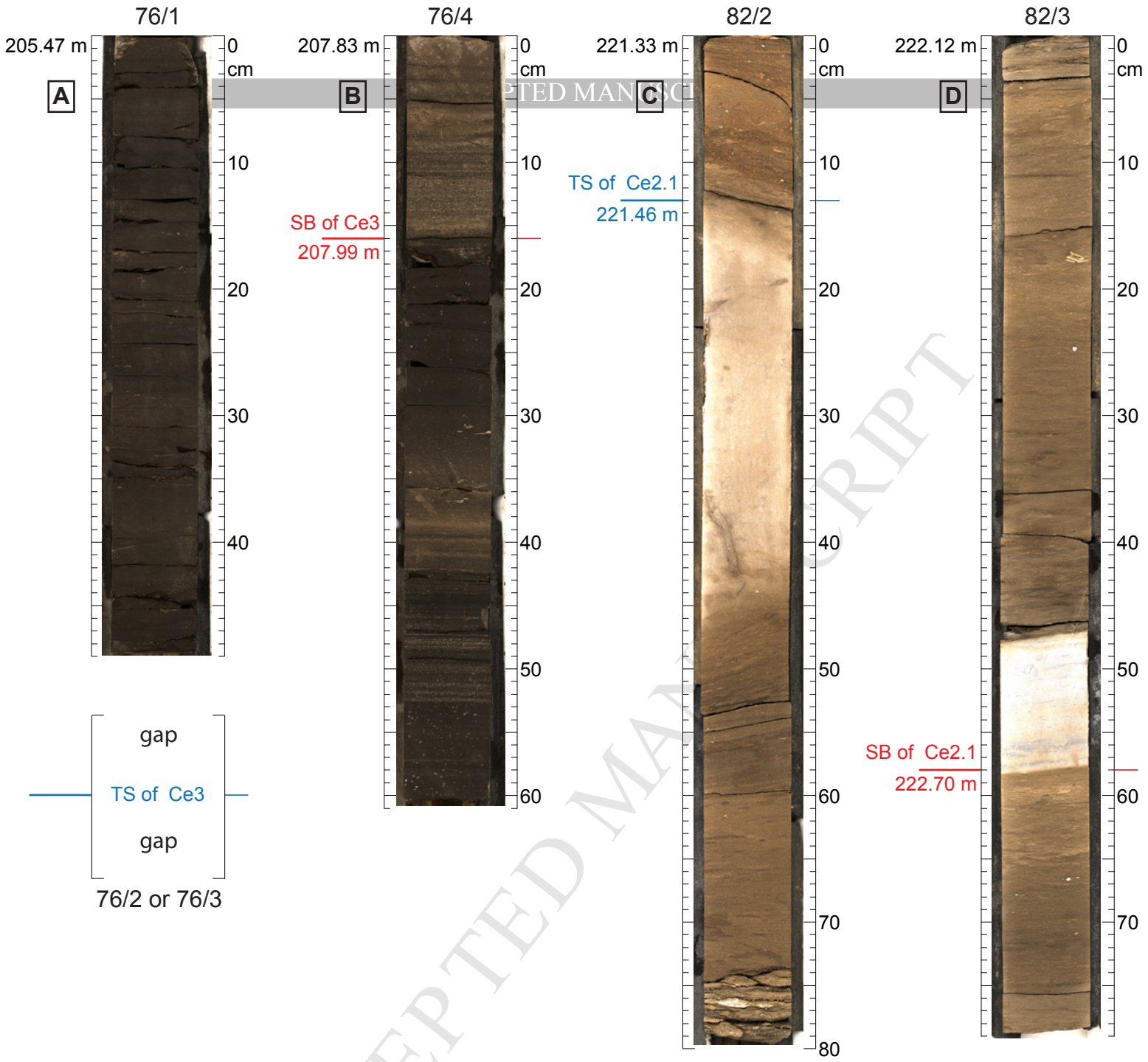

Figure 10A

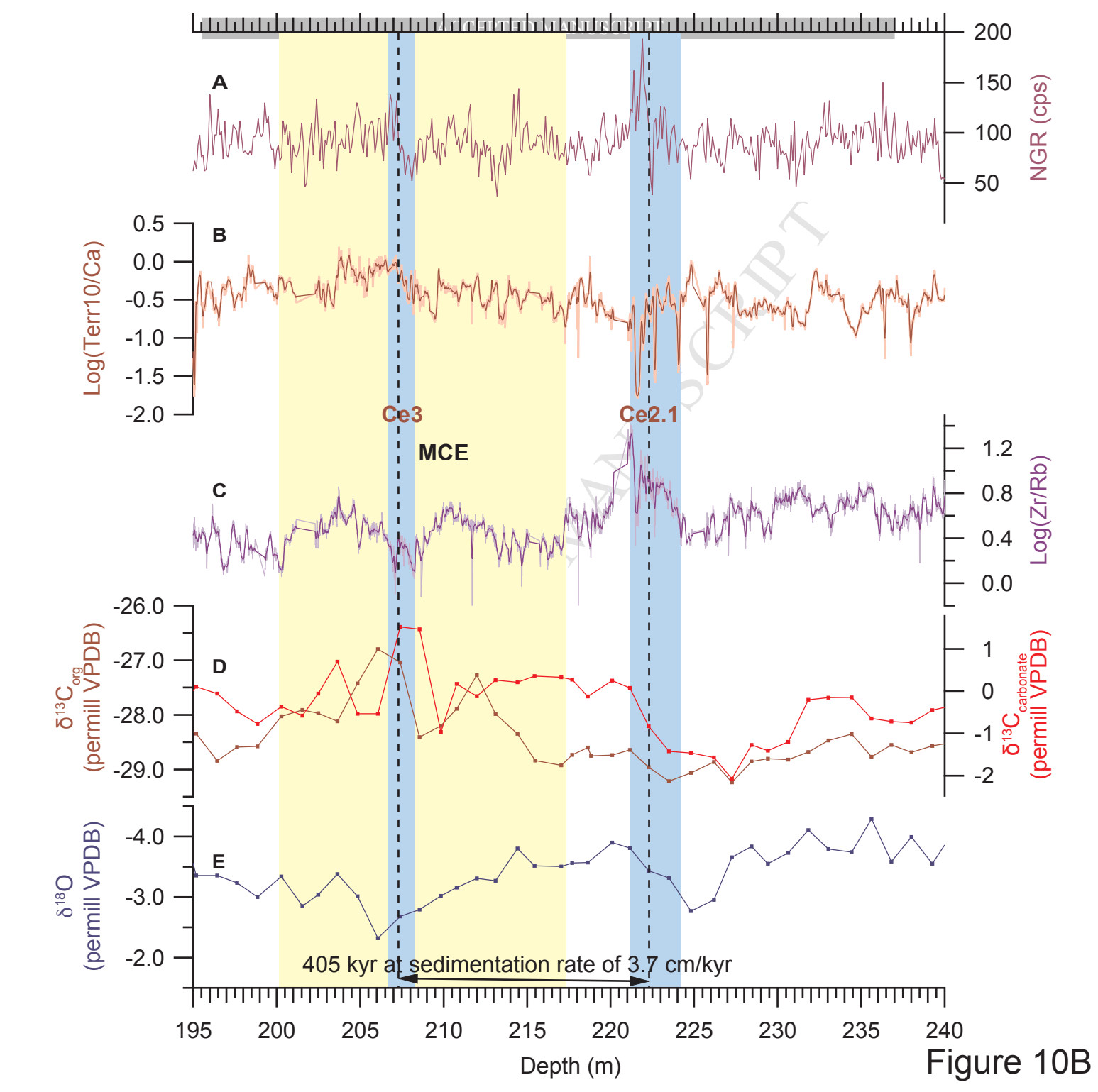
A
B
C
D
E
NGR (cps)
Log(Terr10/Ca)
Log(Zr/Rb)
δ13Corg (permill VPDB)
δ13Ccarbonate (permill VPDB)
δ18O (permill VPDB)
Ce3
Ce2.1
MCE
405 kyr at sedimentation rate of 3.7 cm/kyr
Depth (m)
MANUSCRIPT

Figure 10B

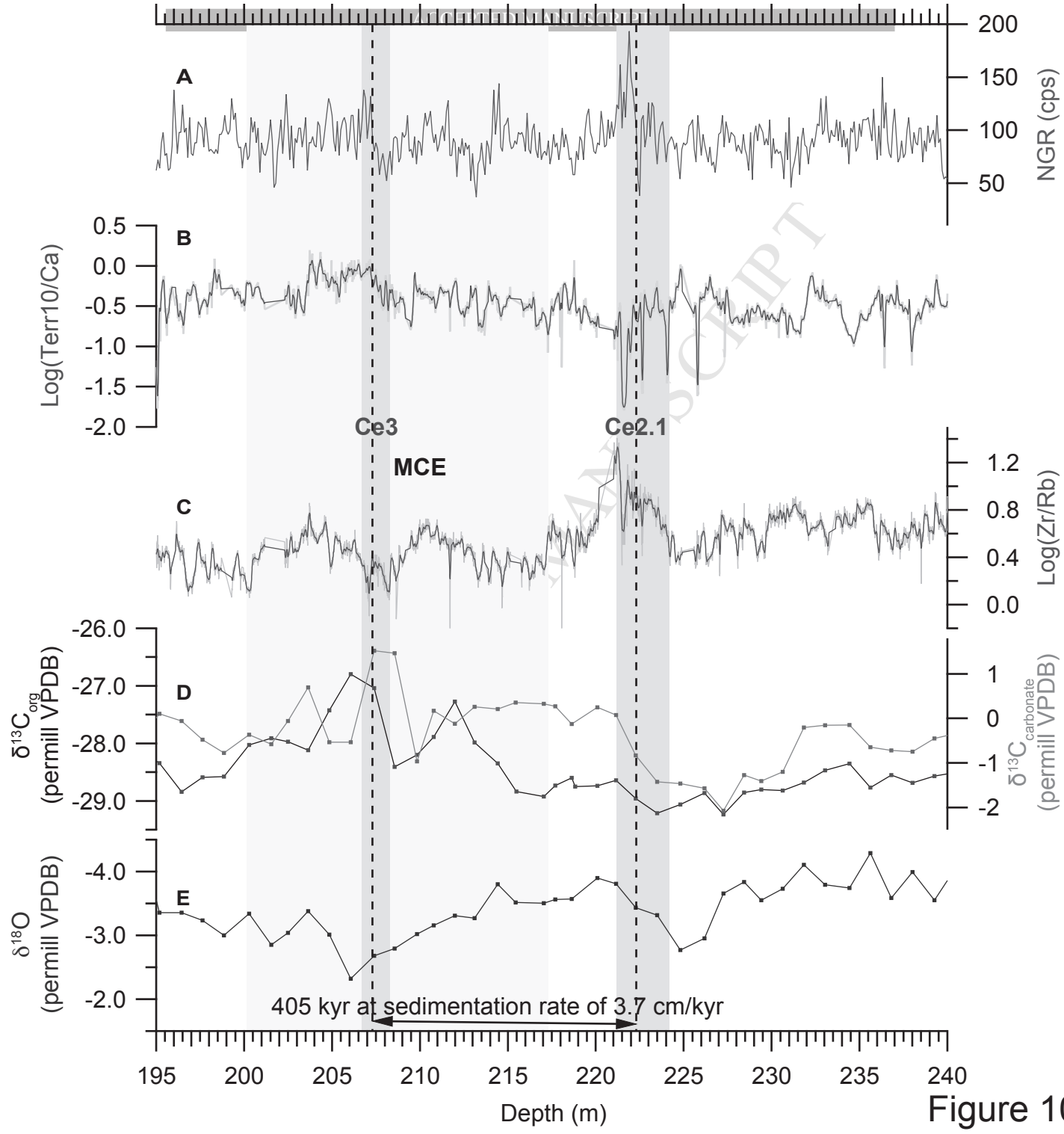
A
B
C
D
E
NGR (cps)
Log(Terr10/Ca)
Log(Zr/Rb)
Ce3
Ce2.1
MCE
δ13Corg (permill VPDB)
δ13Ccarbonate (permill VPDB)
δ18O (permill VPDB)
405 kyr at sedimentation rate of 3.7 cm/kyr
Depth (m)

Figure 10B

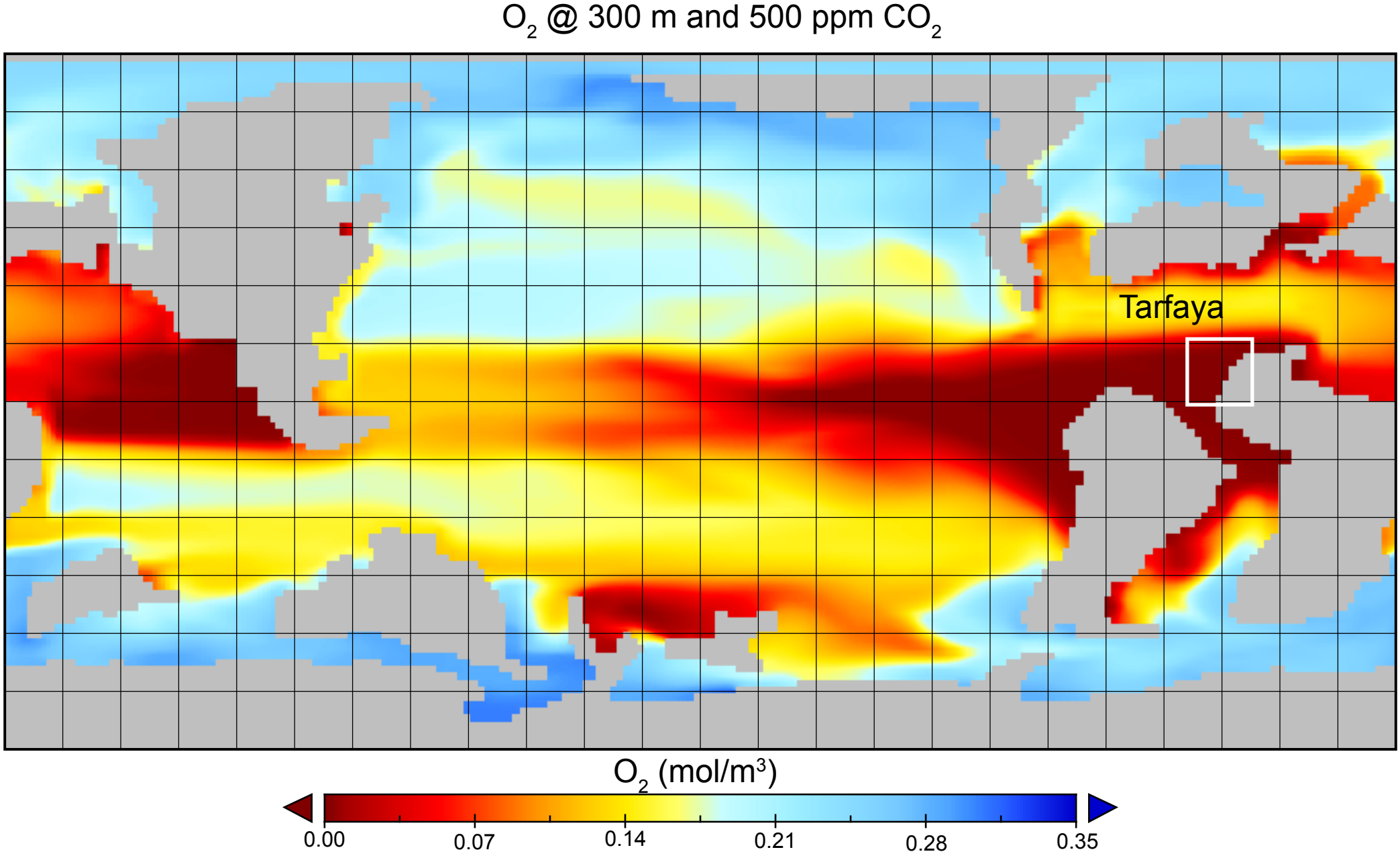
O_2 @ 300 m and 500 ppm CO_2
Tarfaya
O_2 (mol/m^3)
0.00
0.07
0.14
0.21
0.28
0.35

Figure 1

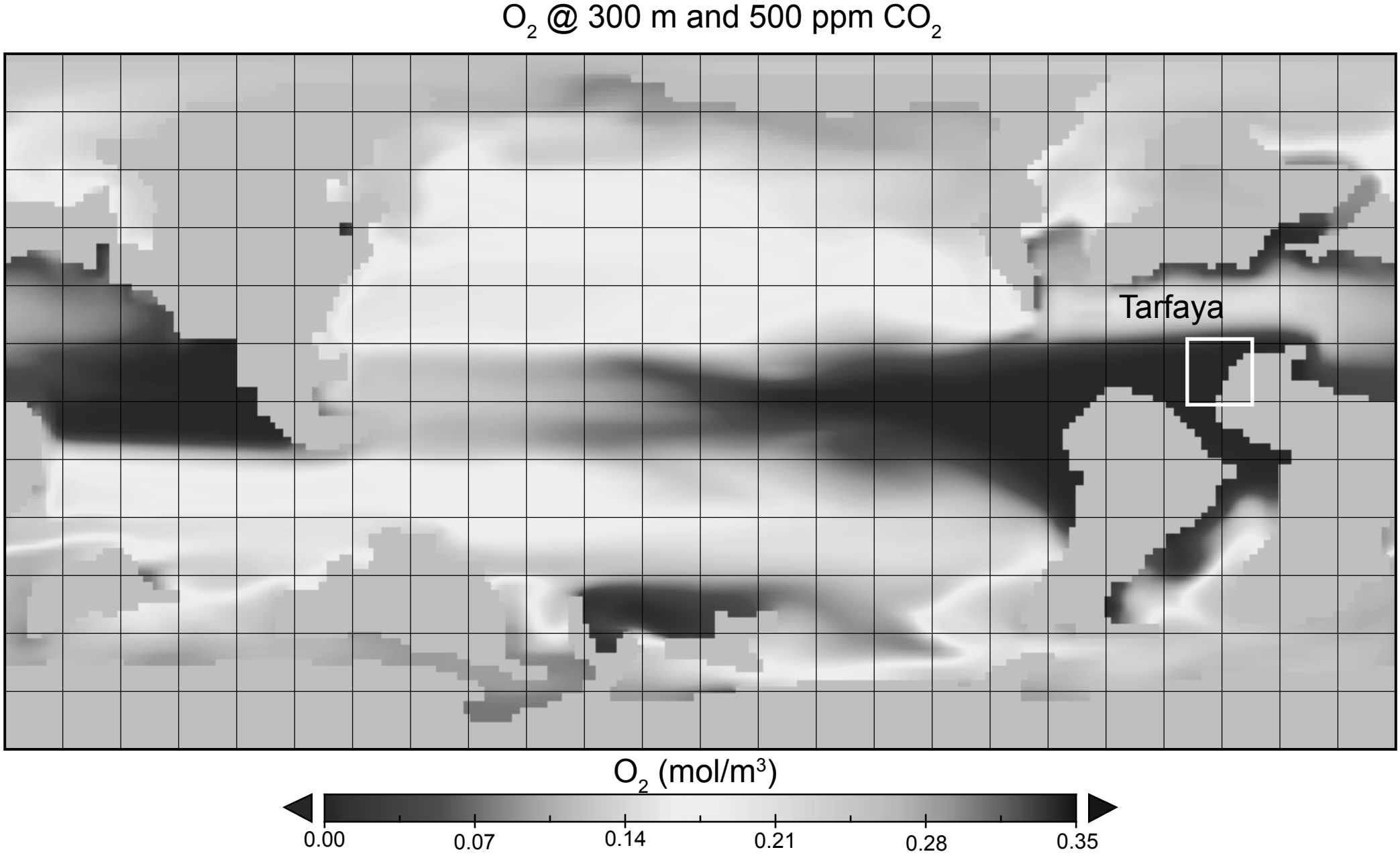
O_2 @ 300 m and 500 ppm CO_2
Tarfaya
O_2 (mol/m^3)
0.00
0.07
0.14
0.21
0.28
0.35

Figure 1

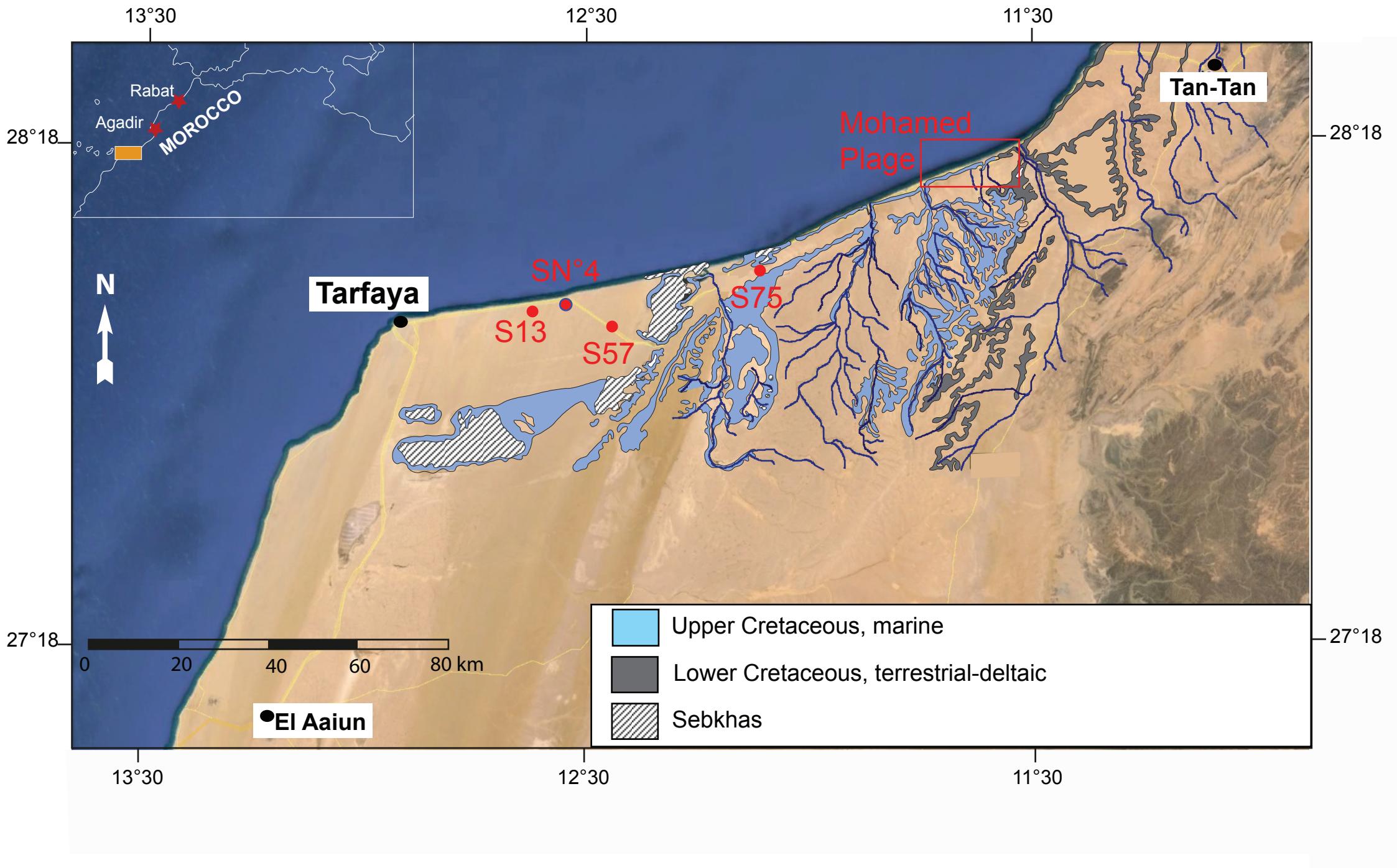

Figure 2

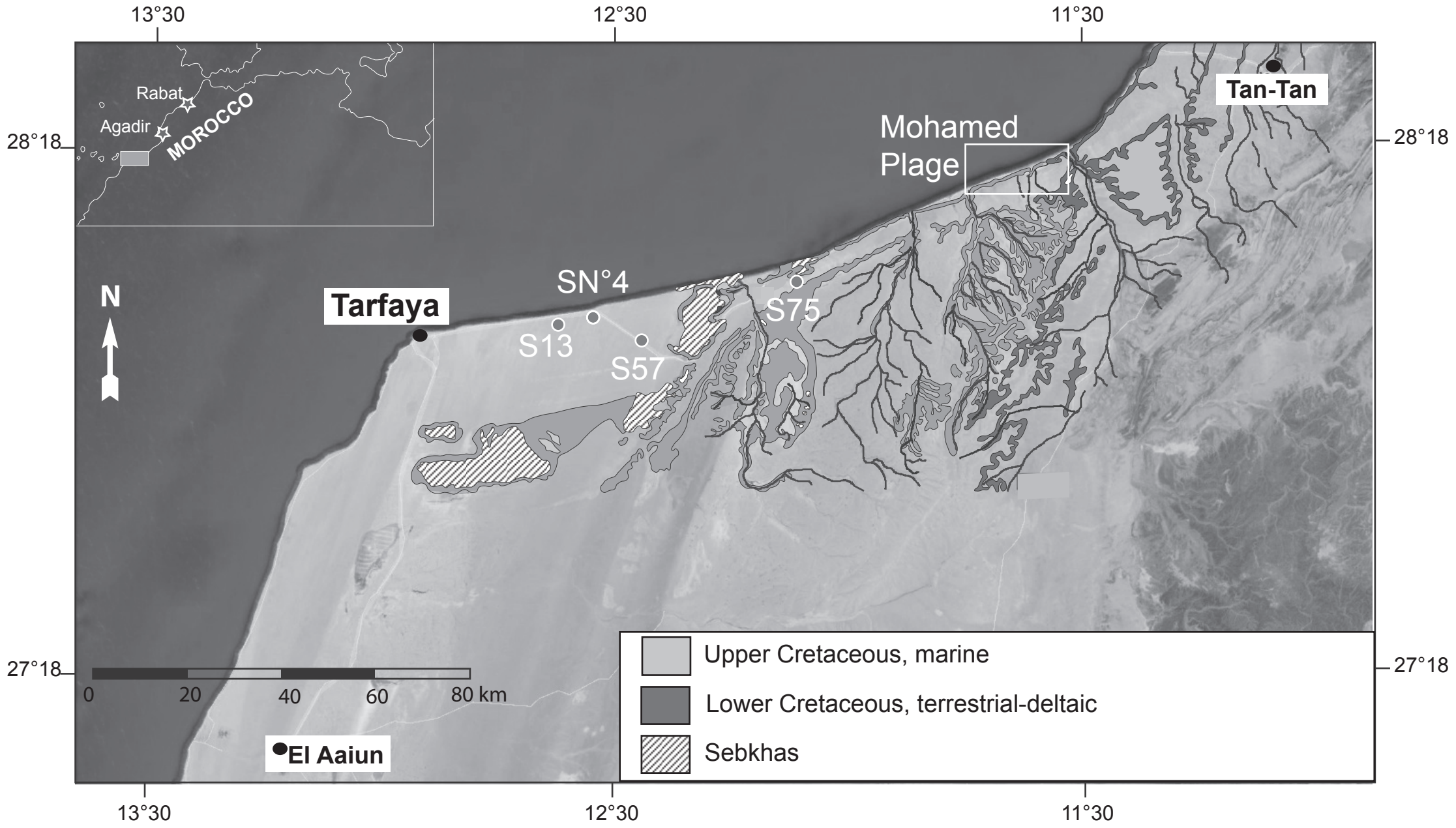
13°30
12°30
11°30
28°18
27°18
Rabat
Agadir
MOROCCO
Mohamed
Plage
Tan-Tan
N
Tarfaya
SN°4
S13
S57
S75
0
20
40
60
80 km
El Aaiun
Upper Cretaceous, marine
Lower Cretaceous, terrestrial-deltaic
Sebkhas

Figure 2

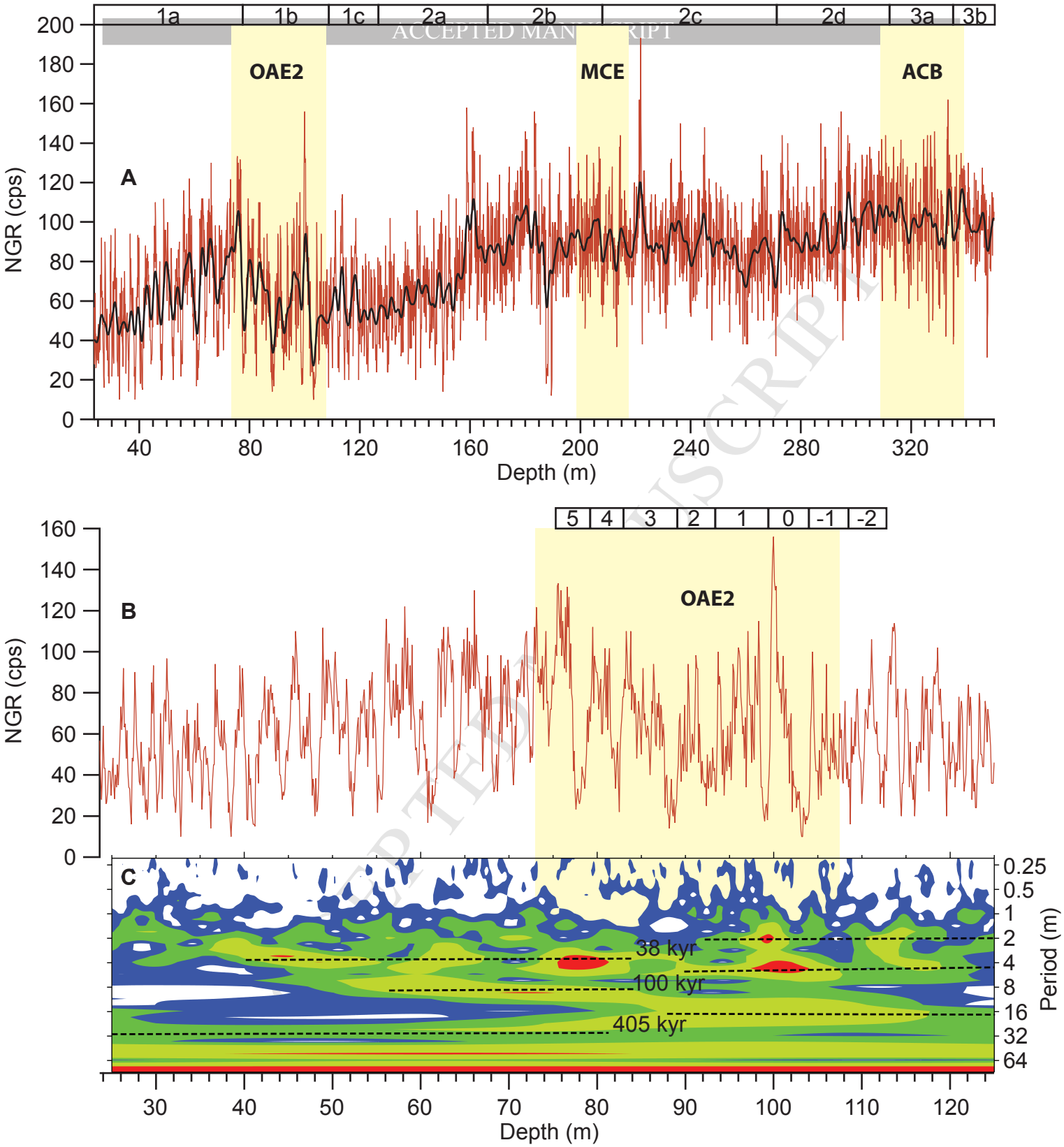
1a
1b
1c
2a
2b
2c
2d
3a
3b
OAE2
MCE
ACB
A
NGR (cps)
Depth (m)
5
4
3
2
1
0
-1
-2
B
OAE2
C
38 kyr
100 kyr
405 kyr
Period (m)
0.25
0.5
1
2
4
8
16
32
64

Figure 3

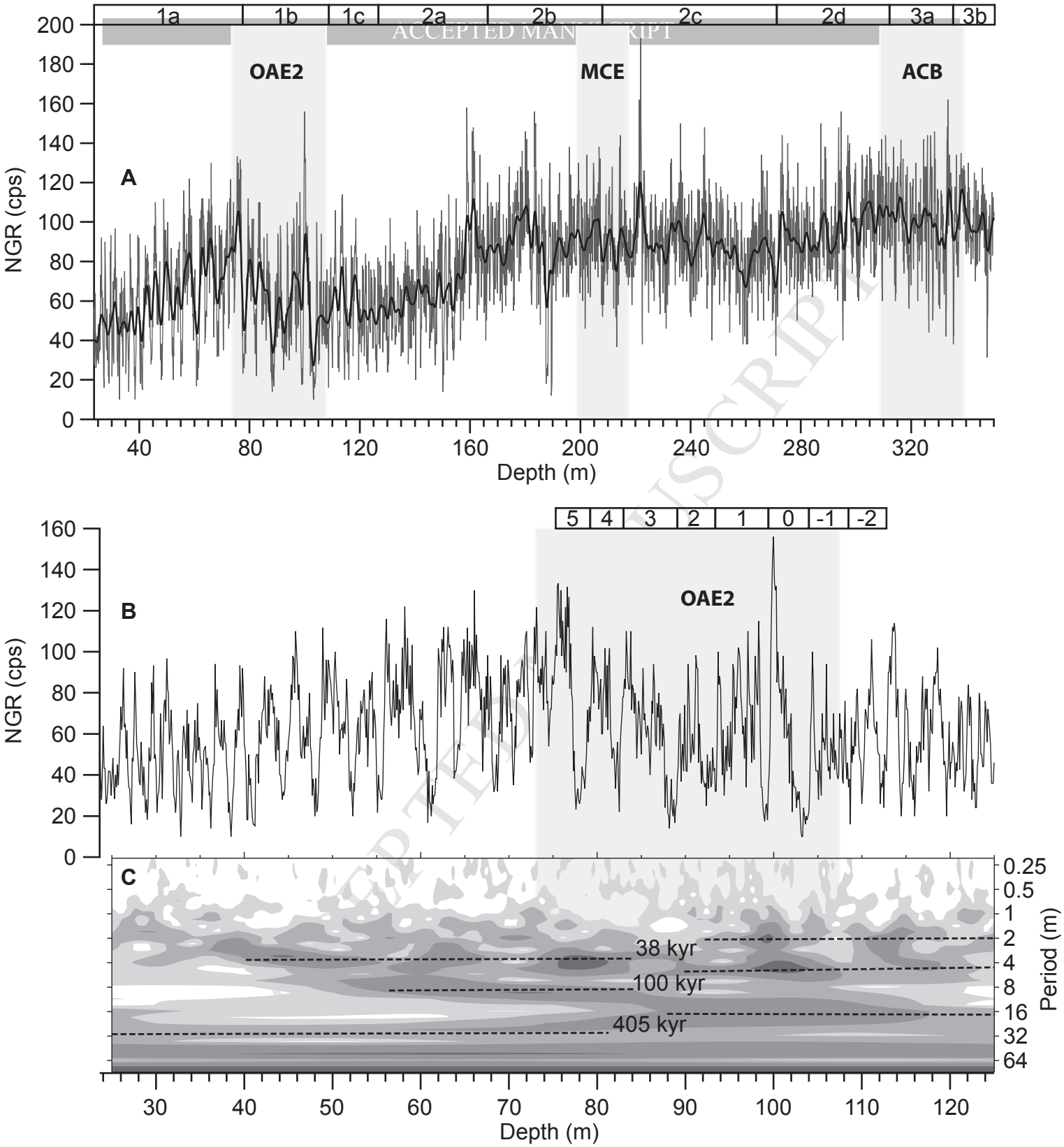
1a
1b
1c
2a
2b
2c
2d
3a
3b
OAE2
MCE
ACB
A
NGR (cps)
Depth (m)
5
4
3
2
1
0
-1
-2
B
OAE2
C
38 kyr
100 kyr
405 kyr
Period (m)
0.25
0.5
1
2
4
8
16
32
64

Figure 3

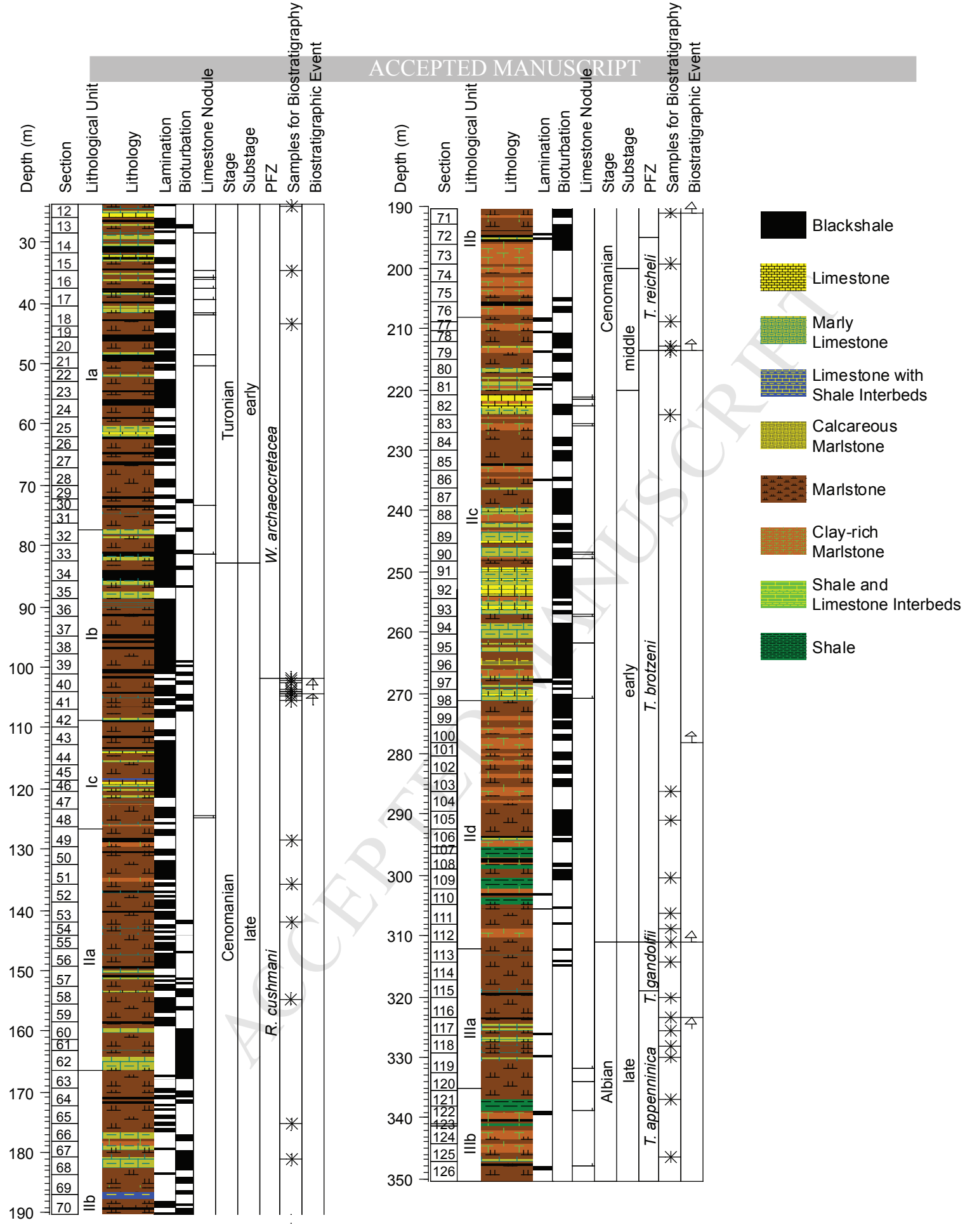

Figure 4A

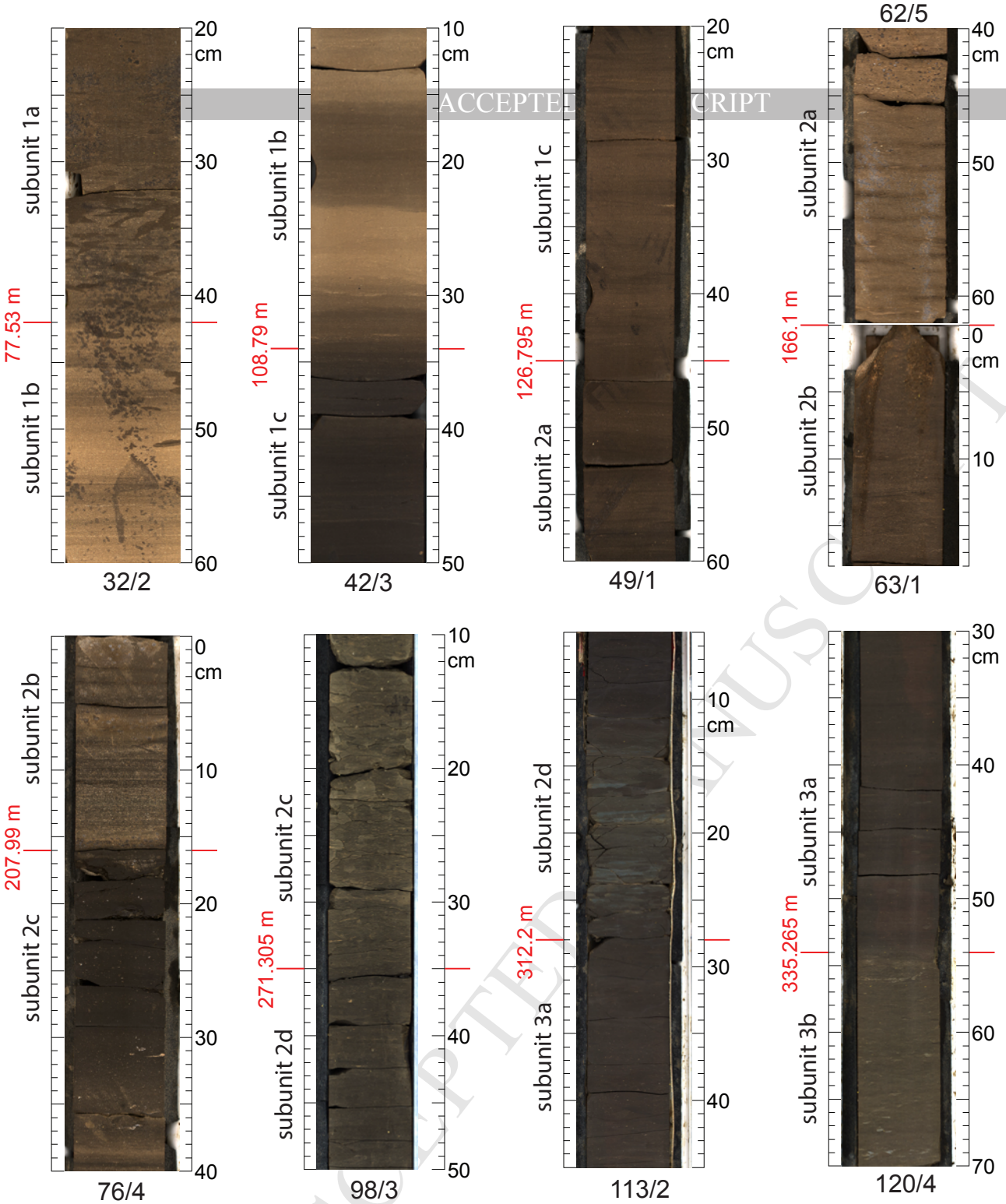

Figure 4B

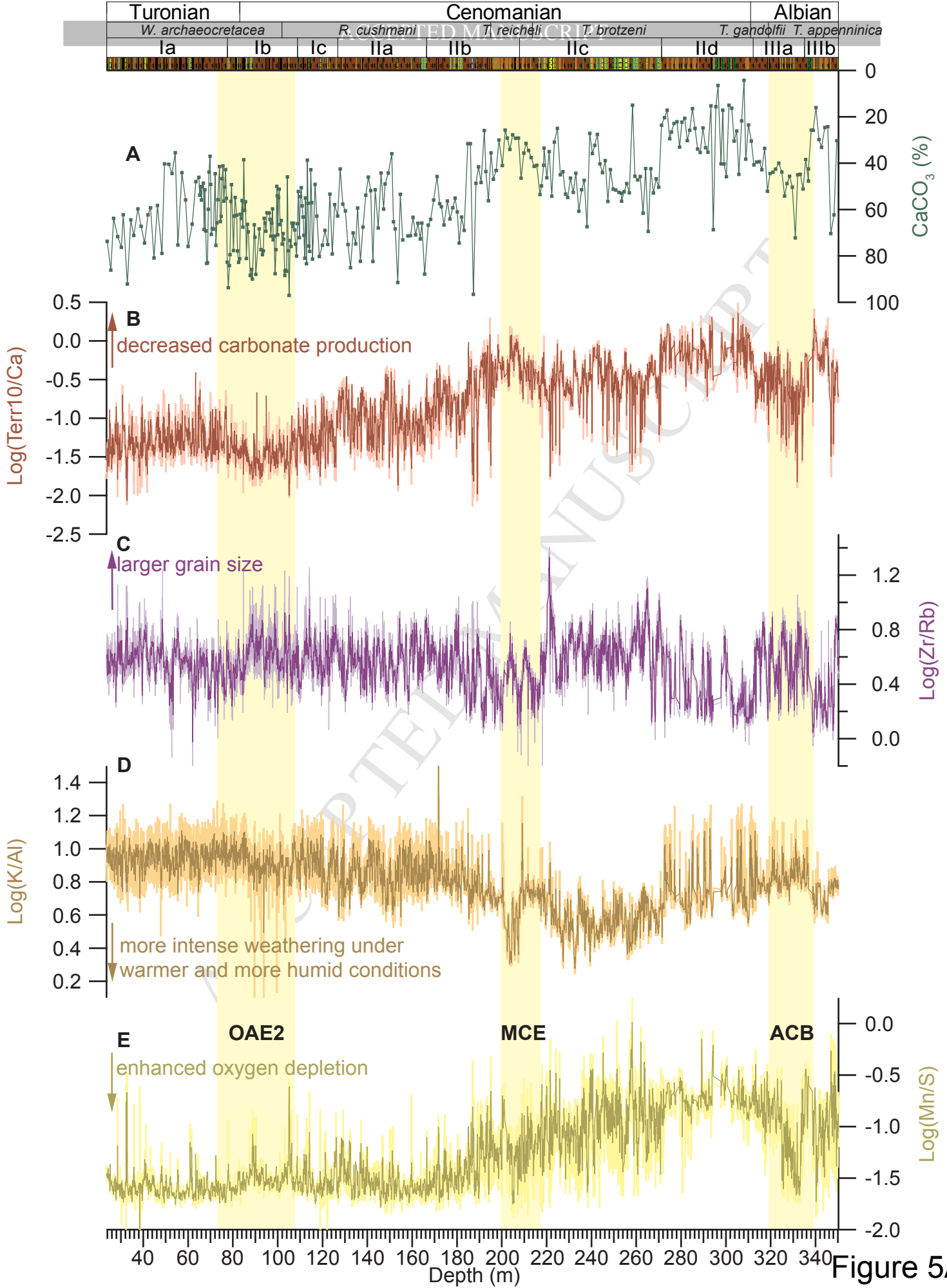
Turonian
Cenomanian
Albian
W. archaeocretacea
R. cushmani
T. reicheli
T. brotzeni
T. gandolfii
T. appenninica
Ia
Ib
Ic
IIa
IIb
IIc
IId
IIIa
IIIb
A
CaCO3 (%)
0
20
40
60
80
100
B
decreased carbonate production
Log(Terr10/Ca)
0.5
0.0
-0.5
-1.0
-1.5
-2.0
-2.5
C
larger grain size
Log(Zr/Rb)
1.2
0.8
0.4
0.0
D
Log(K/Al)
1.4
1.2
1.0
0.8
0.6
0.4
0.2
more intense weathering under
warmer and more humid conditions
OAE2
MCE
ACB
E
enhanced oxygen depletion
Log(Mn/S)
0.0
-0.5
-1.0
-1.5
-2.0
40
60
80
100
120
140
160
180
200
220
240
260
280
300
320
340
Depth (m)

Figure 5A

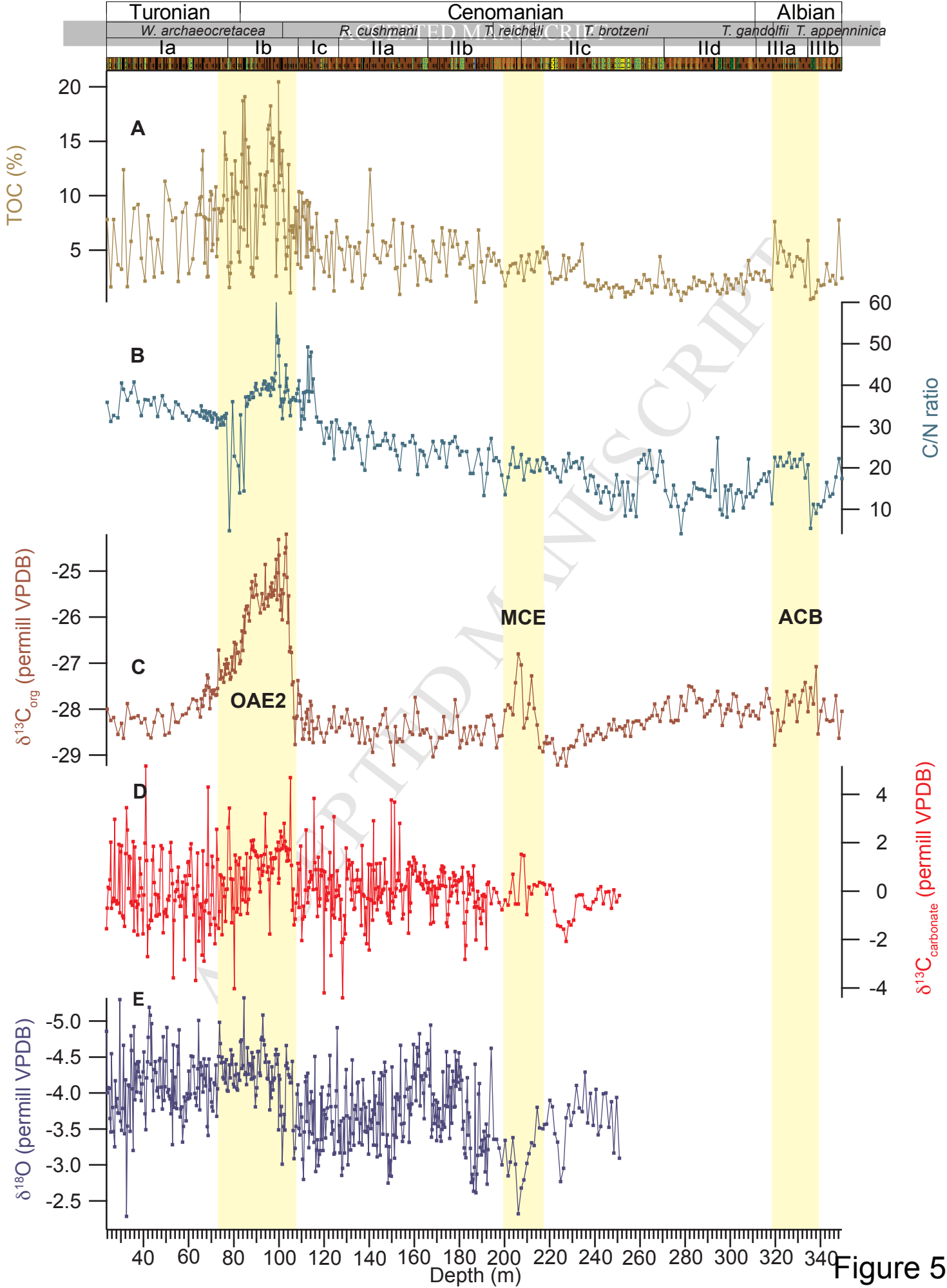
Turonian
Cenomanian
Albian
W. archaeocretacea
R. cushmani
T. reicheli
T. brotzeni
T. gandolfii
T. appenninica
Ia
Ib
Ic
IIa
IIb
IIc
IId
IIIa
IIIb
A
TOC (%)
B
C/N ratio
C
$\delta^{13}C_{org}$ (permill VPDB)
MCE
ACB
OAE2
D
$\delta^{13}C_{carbonate}$ (permill VPDB)
E
$\delta^{18}O$ (permill VPDB)
Depth (m)

Figure 5B

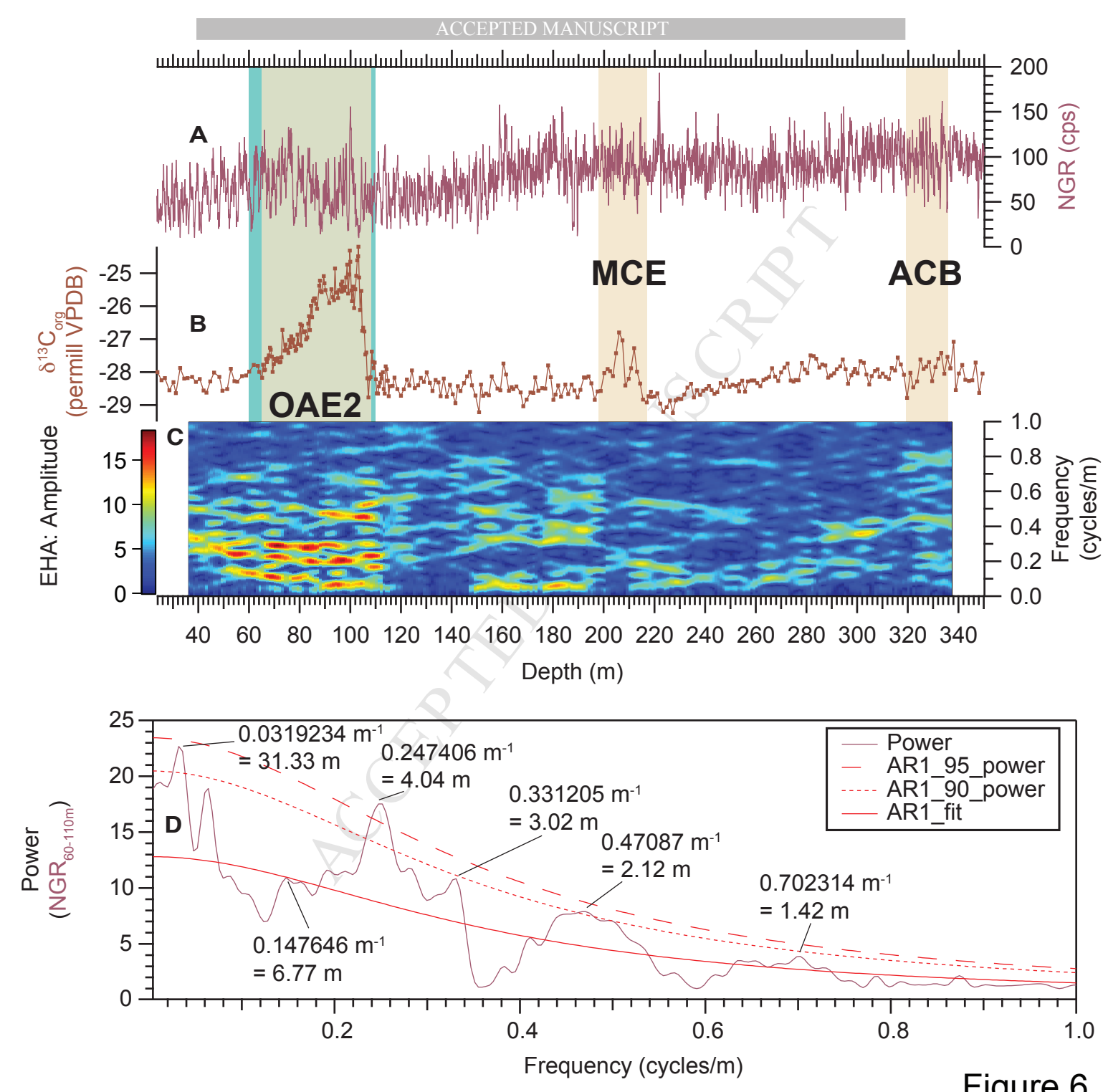

Figure 6

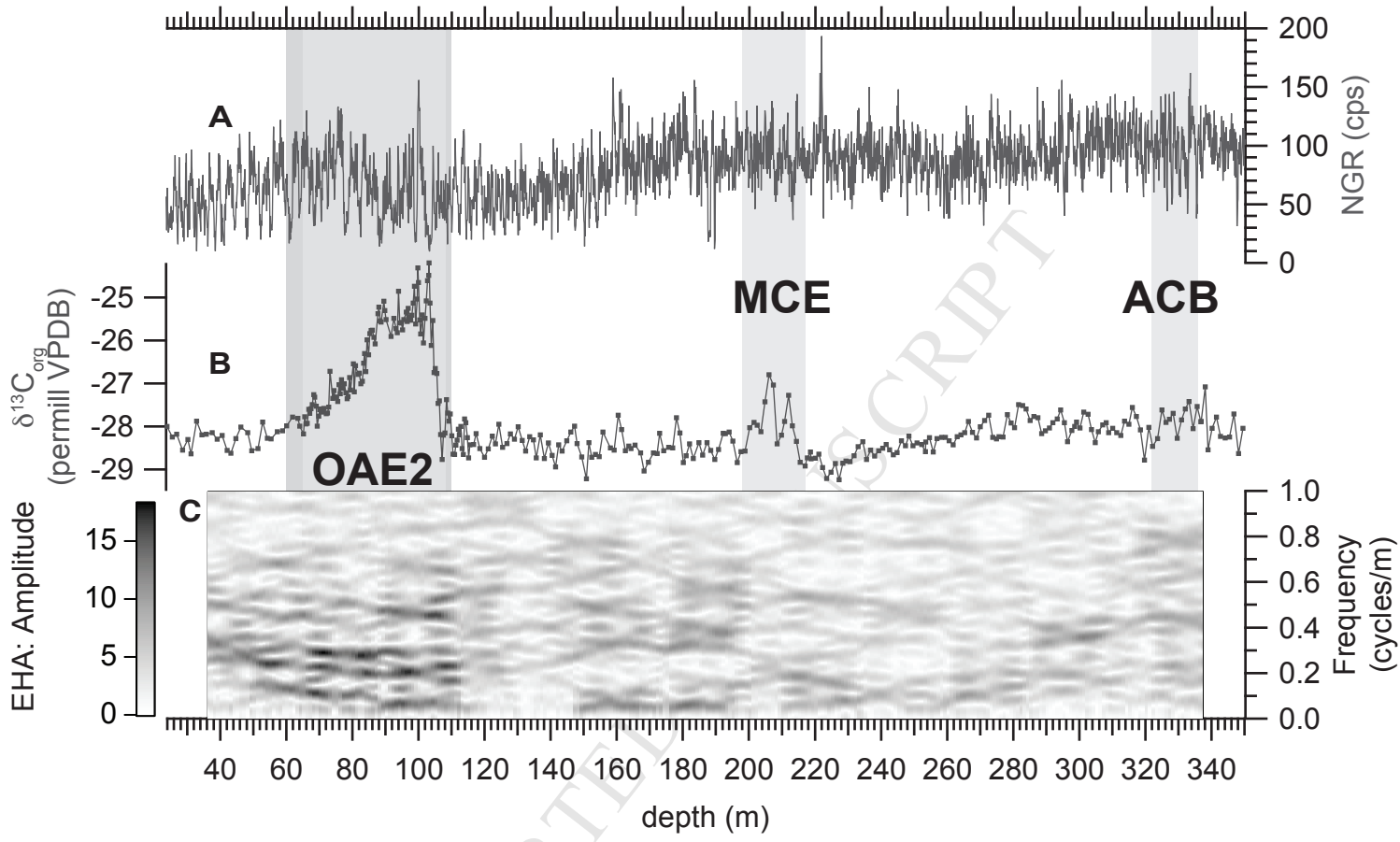

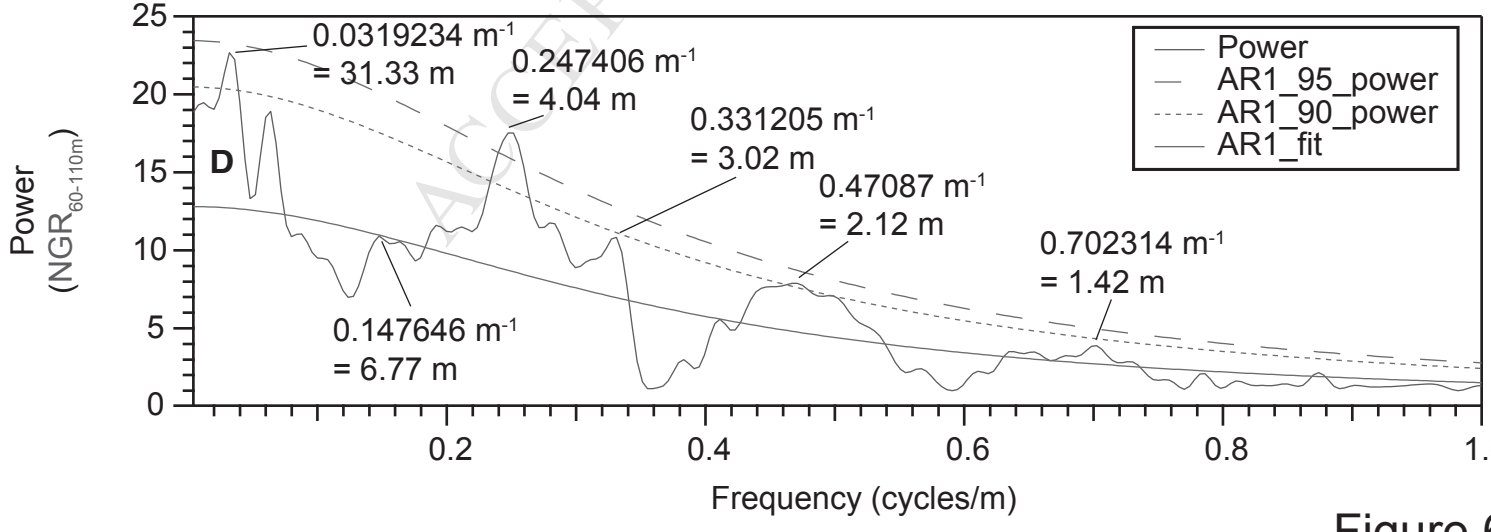

Figure 6

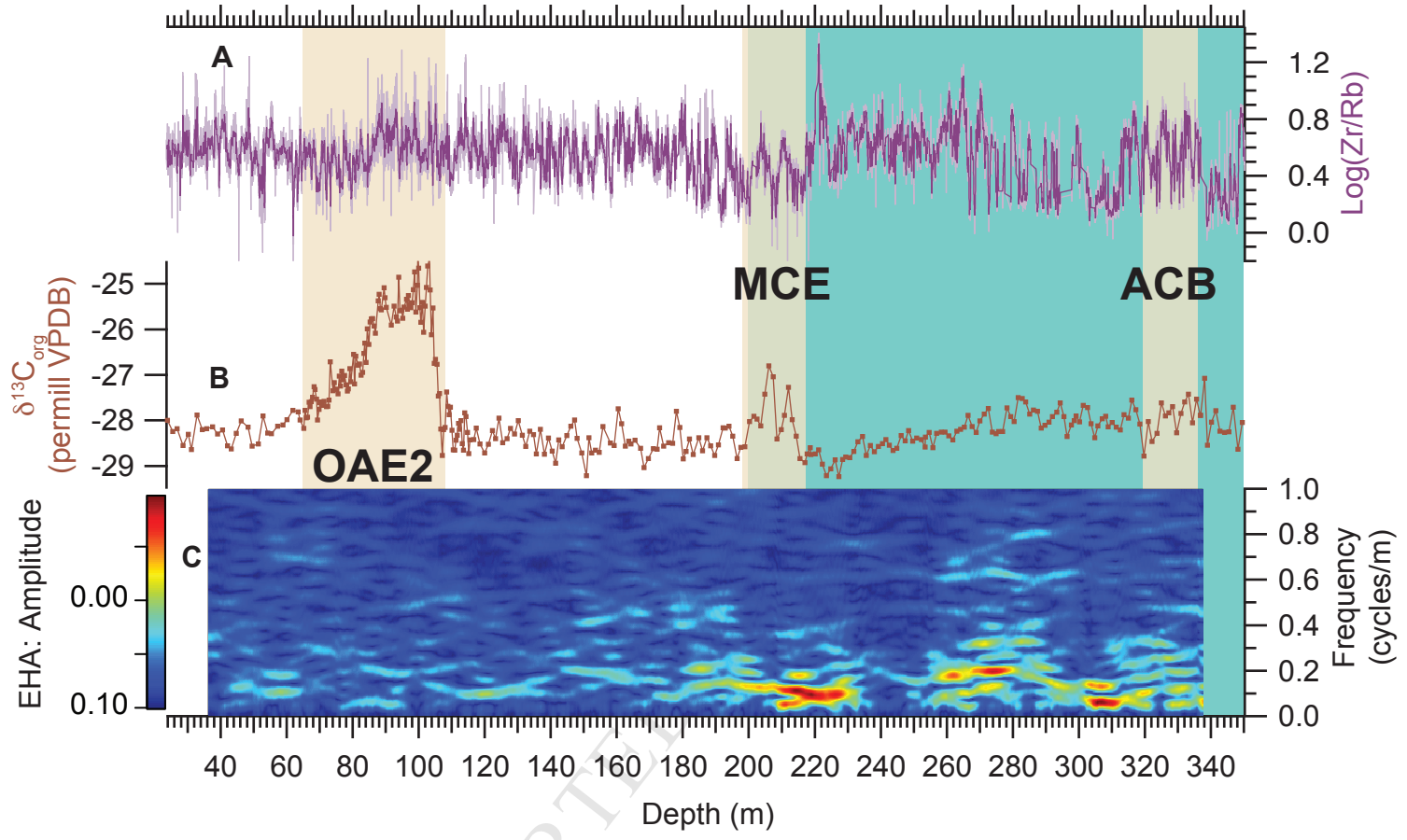

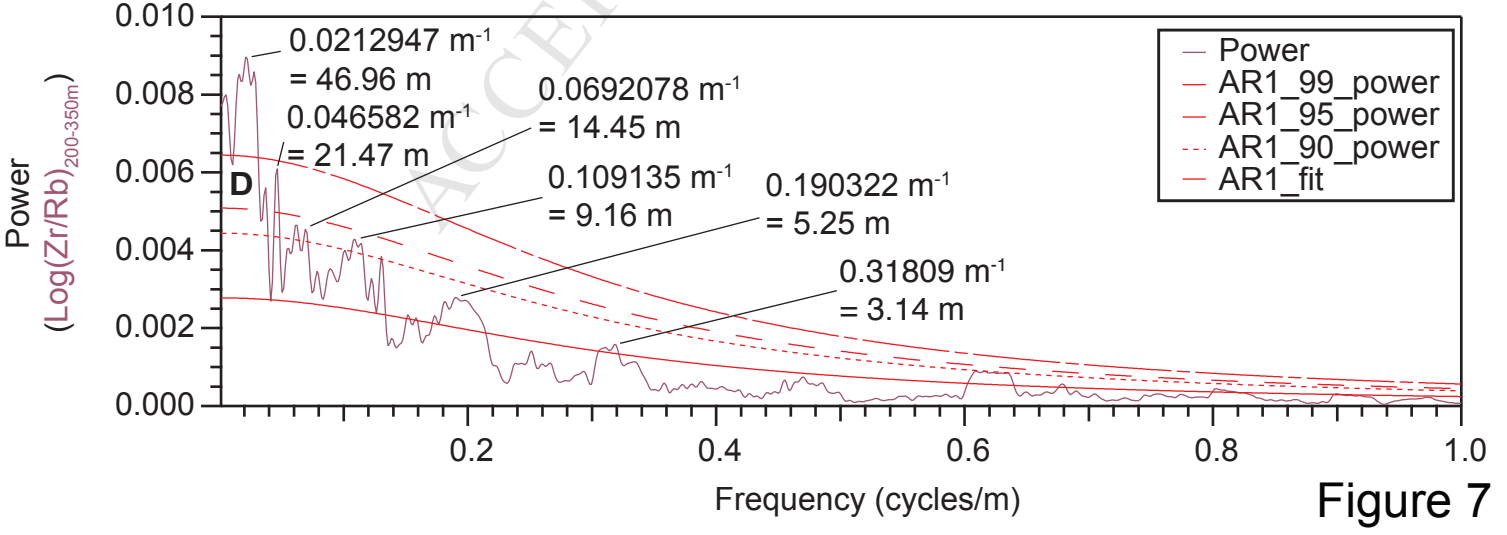

Figure 7

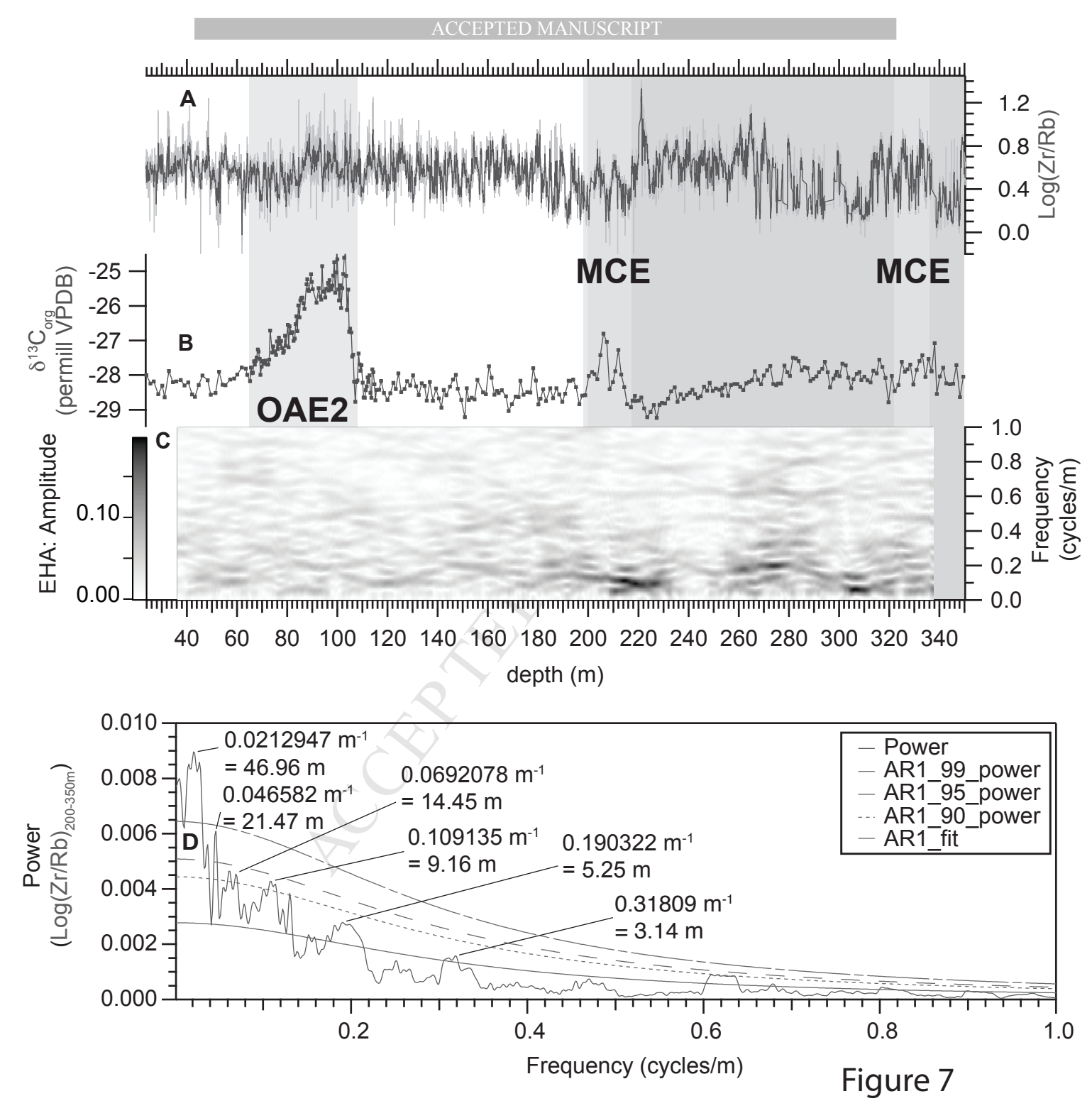

Figure 7

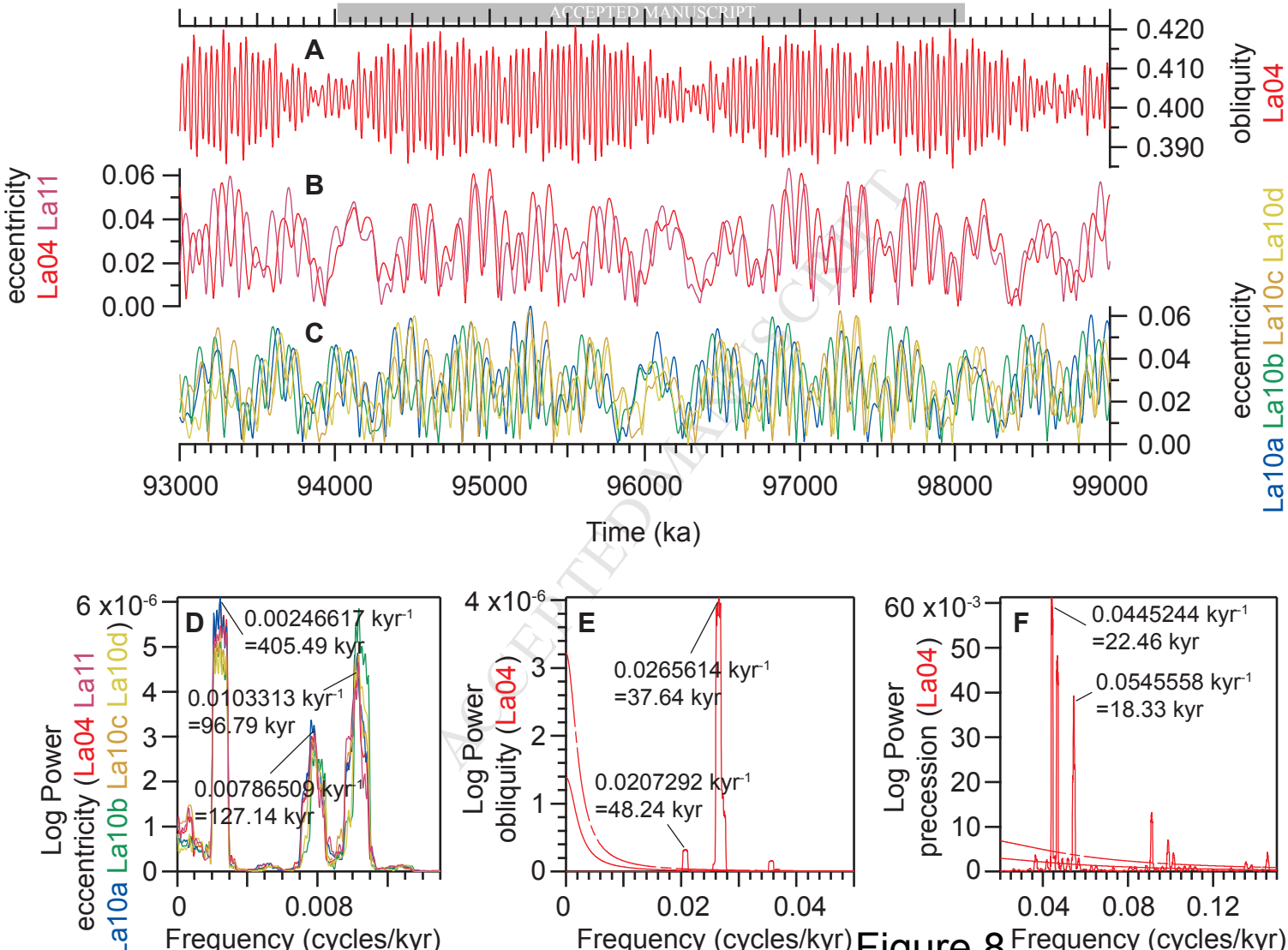

Figure 8

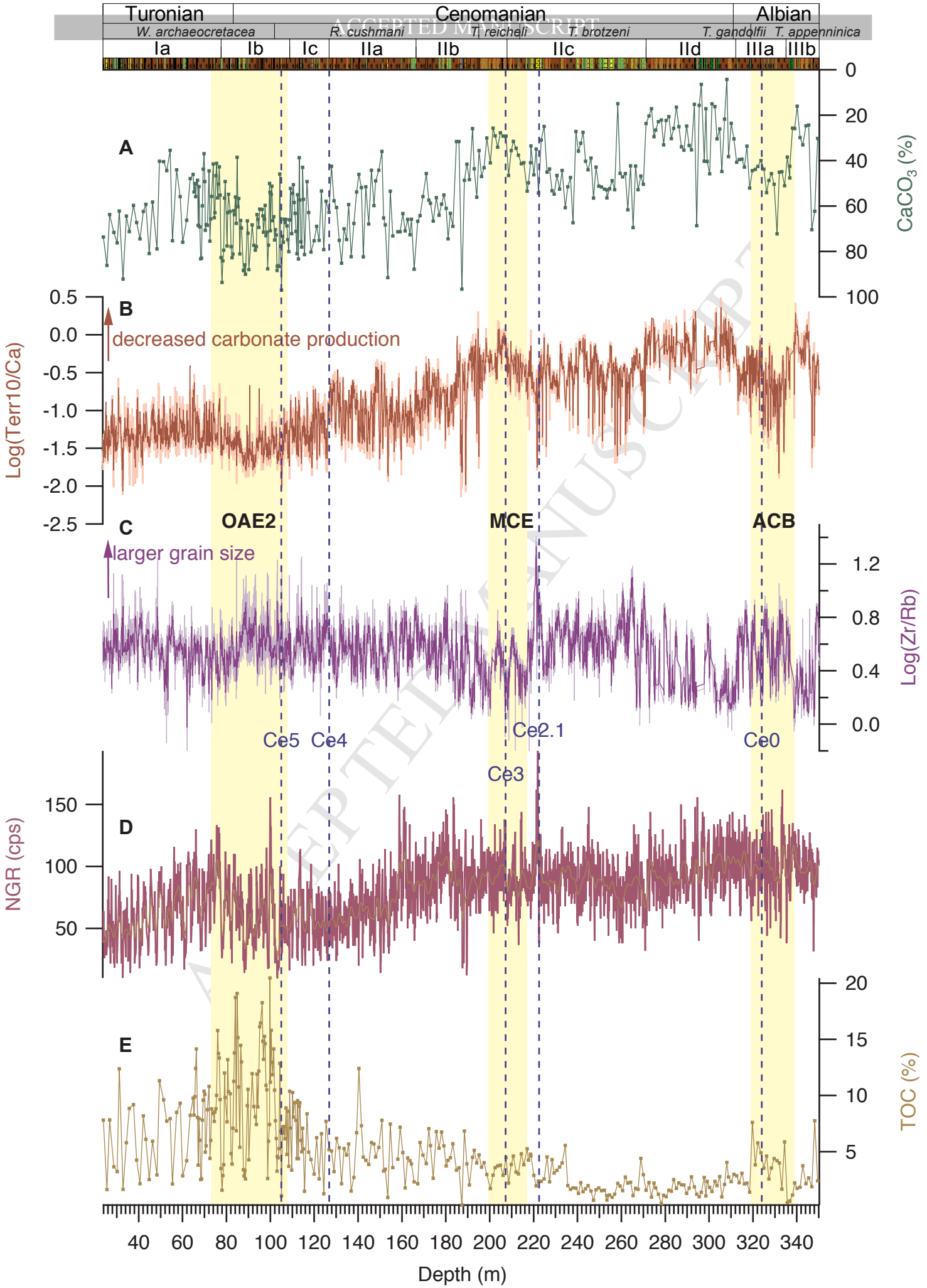
Turonian
Cenomanian
Albian
W. archaeocretacea
R. cushmani
T. reicheli
T. brotzeni
T. gandolfii
T. appenninica
Ia
Ib
Ic
IIa
IIb
IIc
IId
IIIa
IIIb
A
B
C
D
E
decreased carbonate production
larger grain size
OAE2
MCE
ACB
Ce5
Ce4
Ce3
Ce2.1
Ce0
CaCO3 (%)
Log(Terr10/Ca)
Log(Zr/Rb)
NGR (cps)
TOC (%)
Depth (m)
0
20
40
60
80
100
0.5
0.0
-0.5
-1.0
-1.5
-2.0
-2.5
1.2
0.8
0.4
0.0
150
100
50
20
15
10
5
40
60
80
100
120
140
160
180
200
220
240
260
280
300
320
340

Figure 9

Highlights:

Complete upper Albian to early Turonian climate archive in drilled core from Tarfaya Basin

Eccentricity pacing of mid Cretaceous OAE isotope excursions

MCE and OAE2 associated with climate cooling and sea level fall